



– Version of 29 April 2019 –

Very high-resolution modelling of submesoscale turbulent patterns and processes in the Baltic Sea

Reiner Onken¹, Burkard Baschek¹, and Ingrid M. Angel-Benavides¹

¹Helmholtz-Zentrum Geesthacht, Max-Planck-Straße 1, 21502 Geesthacht, Germany

Correspondence to: Reiner.Onken@hzg.de

Abstract. In order to simulate submesoscale turbulent patterns and processes (STPPs) and to analyse their properties and dynamics, the Regional Ocean Modeling System (ROMS) is applied to a subregion of the Baltic Sea around the island of Bornholm. The modeled STPPs provide an aid for the interpretation of observations that were taken during the “Expedition Clockwork Ocean” in the same region in June 2016. To create a realistic mesoscale and submesoscale environment, ROMS with
5 500-m horizontal resolution is one-way nested into an existing operational model. The comparison of the results with satellite images shows good agreement. STPPs with horizontal scales < 1 km are resolved with a second nest of 100-m resolution providing a deep insight into ageostrophic processes and associated quantities. STPPs evolve rapidly within a about a day. They are characterised by strong vertical speeds of $\mathcal{O}(100)$ m day⁻¹ and relative vorticities and divergences reaching multiple of the Coriolis parameter. Typical elements of the secondary circulation of two-dimensional strain-induced frontogenesis are
10 identified at an exemplary front in shallow water, and details of the ageostrophic flow field are revealed. The conditions for inertial and symmetric instability are evaluated for the whole domain, and the components of the tendency equation are computed in a subregion. While anticyclonic eddies are generated solely along coasts, cyclonic eddies are rolled-up streamers and found in the entire domain. A special feature of the cyclones is their ability to absorb internal waves and to sustain patches of continuous upwelling for several days favouring plankton growth. The kinematic properties show good agreement
15 with observations, while some observed details within a small cyclonic eddy are only partly reproduced, most likely due to a lack of horizontal resolution or non-hydrostatic effects.

1 Introduction

An ambitious expedition was conducted in the Baltic Sea in June 2016 under the lead of the Helmholtz-Zentrum Geesthacht (HZG). The objective of the “Expedition Clockwork Ocean” was to observe submesoscale patterns and processes (STPPs) in
20 order to better understand their role in the cascade of turbulent kinetic energy in the ocean, and to assess their impact on the primary production. In this article, high-resolution modeling is used to understand and interpret the observed features.

Submesoscale turbulence is characterised by horizontal scales between 10 m and 10 km, vertical scales from 1 to 100 m, and time scales from hours to days (McWilliams, 2016). Thus, in the turbulence spectrum of the ocean, the submesoscale occupies 4 orders of magnitude in the horizontal, 3 orders in the vertical, and 3 orders of magnitude in time. As the whole spectrum of



horizontal motions extends over 9 orders of magnitude between the basin-scale circulation (10^6 m) and the dissipation scale (10^{-2} m, see Müller et al. (2005)), a significant fraction of the spectrum is occupied by the submesoscale. The submesoscale wavenumber band is the intermediate regime between the mesoscale and the microscale (McWilliams, 2008); it separates the larger-scale flow, where the Coriolis force dominates (Rossby number, $Ro < 1$), from the smaller scales where the rotation of the Earth is of minor importance ($Ro \sim \mathcal{O}(1)$).

The energy sources for ocean currents are mainly at the planetary scale ($\mathcal{O}(1000$ km)), while the energy is removed at the microscale by viscous dissipation of kinetic energy where it is finally converted to heat. In order to equilibrate the ocean on climatological time scales, this demands a continuous spectral flow from the planetary scale to the microscale, which is called the “blue” cascade. However, according to the theory of geostrophic turbulence (Charney, 1971; Rhines, 1979), the energy cascade in low Rossby number regimes is “red”, i.e. there is a feedback of energy from mesoscale turbulence to larger scales. This leads to the question how the mesoscale energy is dissipated. A generic answer was given by McWilliams (2016): “Submesoscale currents spontaneously emerge from mesoscale eddies and boundary currents, especially in the surface and bottom boundary layers. They are generated through instabilities, frontogenesis and topographic wakes” leading to the required forward cascade.

The elements of submesoscale turbulence are essentially the same as in mesoscale turbulence: fronts, instabilities, meanders, eddies, and filaments. However, the submesoscale spatio-temporal scales are 1 or 2 orders of magnitude smaller. The first observational campaigns targeting explicitly at the characteristics of STPPs were the Lateral Mixing experiment (LatMix) in the North Atlantic (Shcherbina et al., 2015) and the Submesoscale Experiments (SubEx) in the Southern California Bight (Ohlmann et al., 2017).

More detailed knowledge about the generation, kinematics, and dynamics of STPPs is conveyed by experiments with offline nested numerical models, so far predominantly applied to the regimes of eastern and western boundary currents. Using an idealised ROMS (Regional Ocean Modeling System, Shchepetkin and McWilliams (2005)) model with a flat bottom, a straight coast line, and uniform wind stress, Capet et al. (2008a, b, c) investigated the mesoscale to submesoscale transition in the California Current system. Based on 5 different model setups with variable horizontal resolution ranging from 12 to 0.75 km, they found that vigorous STPPs develop as the horizontal grid scale was reduced to $\mathcal{O}(1)$ km. The STPPs are initialised by the generation of submesoscale fronts that are strained between mesoscale eddies. Some of these fronts become unstable, develop submesoscale meanders, and fragment into roll-up vortices. These processes are accompanied by vertical velocities up to 50 m day^{-1} and by relative vorticity values of $\mathcal{O}(f)$, where f is the Coriolis parameter. Computations of the energy balance showed that significant conversion from potential to kinetic energy (baroclinic instability) takes place, both in the mesoscale and submesoscale waveband. A significant forward energy cascade occurs in the submesoscale range in transit to dissipation at the microscale. Using ROMS at very high horizontal resolution (150 m) and with realistic topography, Gula et al. (2016a) studied the submesoscale structure in the interior of a mesoscale cyclonic eddy that was generated on the inshore side of the Gulf Stream interacting with the shelf slope. The model results revealed multiple submesoscale fronts at the rim of the eddy that appear as elongated vorticity filaments, reaching locally multiple of f . Like in the California Current System, these filaments become unstable and break up into strings of submesoscale vortices that are advected into the interior of the mesoscale eddy. There, the cyclonic vortices are associated with low-salinity patches, indicating upwelling. Furthermore, it was shown that the



divergence of the flow is dominated by intense small-scale patterns. These patterns are partially associated with the genesis of multiple fronts, but exhibit also characteristics of internal gravity waves propagating away from mesoscale fronts. In another article, Gula et al. (2014) investigated the life cycle of a submesoscale cold filament on the South Wall of the Gulf Stream: the formation of the filament (filamentogenesis) is primarily caused by an intensification of surface buoyancy gradients due to horizontal straining flows and a two-celled ageostrophic secondary circulation with strong surface convergence and associated downwelling in the centre.

The theory of frontogenesis and the associated secondary circulation is significantly shaped by the meteorological literature (e.g. Eliassen (1962)) where a front is formed in the confluence zone of a deformation field (Fig. 9.1b in Holton (1982)), that is generated in the centre of two crosswise arranged pairs of cyclonic and anticyclonic eddies. Typical characteristics of such a front are an along-front geostrophic jet and a cross-front ageostrophic overturning cell with downwelling on the dense side and upwelling on the less dense side of the front. For mesoscale fronts, this picture was authenticated by the idealised model studies of Bleck et al. (1988), Nagai et al. (2006), and Thompson (2000). For submesoscale fronts, the very recent model study of McWilliams (2017) confirms that “These circulation patterns, ..., are qualitatively similar to those due to the ‘classical’ mechanism of strain-induced frontogenesis”.

Baroclinic instability and instabilities driven by the horizontal shear of currents are the main processes leading to the instability of submesoscale fronts. The solutions of the classical problem of baroclinic instability (Charney, 1947; Eady, 1949) sufficiently explain the most unstable wavelength and growth rate of mesoscale disturbances, but these disturbances encompass a large fraction of the water depth including the surface layer and main thermocline. By contrast, another short-wave type of baroclinic instability was described by Blumen (1979) in the case of reduced stratification of the (atmospheric) boundary layer. The oceanic equivalents for this type are inertial (or centrifugal), symmetric, and mixed-layer instability. The latter was thoroughly investigated by Boccaletti et al. (2007) who showed that this class of instabilities may occur in the surface and bottom mixed layer; therefore, it is denoted as “mixed-layer instability”. It is a hybrid instability composed of gravitational and baroclinic instabilities finally leading to a flattening of isopycnals, and a positive (upward) buoyancy flux. It requires lateral buoyancy gradients, and it is composed of short modes between 200 m and 20 km and growth rates around 1 day^{-1} . The starting point for such instabilities is the slumping of isopycnals that is constrained by rotation, because the thermal wind balance is established after a pendulum day. Thereafter, baroclinic instability generates wavelike disturbances that upset the thermal wind balance. As shown by Fox-Kemper and Ferrari (2008), the positive vertical buoyancy flux associated with mixed-layer instability is most important for the restratification of the upper ocean. By contrast, inertial (or centrifugal) instability does not require lateral buoyancy gradients but horizontal shear plus negative absolute vorticity. Therefore, inertial instability is driven by barotropic instability while a vertical buoyancy flux is not necessary. Pure inertial instability is unlikely to occur in the surface mixed layer, but it may arise when currents interact with topography on their right hand side (on the northern hemisphere), creating strong anticyclonic relative vorticity. A necessary condition for the occurrence of inertial instability is a relative vorticity smaller than $-f$ (Haine and Marshall, 1998; Thomas et al., 2013). Symmetric instability is a hybrid gravitational-inertial instability, and may be considered to be a special type of mixed-layer instability. To a first approximation, it arises when the potential vorticity is negative and the Richardson number is $Ri < 1$ (Boccaletti et al., 2007). The numerical simulations of



Haine and Marshall (1998) confirm that symmetric instability dies as soon as $Ri > 1$ and baroclinic instability takes over. The transition from gravitational-inertial to gravitational-baroclinic instability was explored by Stamper and Taylor (2017) in detail. More in-depth conditions for symmetric instability were formulated by Taylor and Ferrari (2009) and Thomas et al. (2013).

Most of the numerical studies cited above manifest that STPPs act as a conveyor for kinetic energy from the mesoscale to the microscale. Besides this role, STPPs are also relevant for primary production (Mahadevan, 2016). In particular, the associated strong upward vertical motions transport nutrients into the sunlit ocean where plankton growth occurs, while carbon fixed by the phytoplankton cells is removed from the euphotic layer by downwelling events (Lévy et al., 2012).

The “Expedition Clockwork Ocean” was conducted 20–28 June 2016. The sea surface temperature of a limited area was first scanned with an infrared camera onboard an aerial motor glider because the location and time of the occurrence of STPPs is not predictable. As soon as a temperature signal of an STPP was localised, various measuring platforms were used for rapid repeat measurements of the three-dimensional structure and the temporal evolution of that feature before its decay within a few hours. Measurements were performed with research vessels, autonomous underwater vehicles, and even a 75-m long zeppelin. The latter “parked” over the STPP in order to record its life cycle with very high-resolution infrared and hyperspectral cameras. (<http://www.uhrwerk-ozean.de>, last access 20 September 2018). In order to reproduce the mesoscale physical environment in the experimental area of the “Expedition Clockwork Ocean”, a ROMS model with 500-m horizontal resolution (referred to as R500 in the following) is nested into an existing coarser-resolution HBM operational model. An even finer nested ROMS model with a grid size of 100 m (R100) is used to enable the generation of STPPs thus providing a base for an analysis of their properties and dynamics, and for comparison with high-resolution observations.

The utilised numerical models are described in Section 2. The results of the numerical experiments are presented in Sections 3 and 4 and compared with observations in Section 5, followed by the conclusions. In the following, all time specifications refer to the year 2016 (unless stated otherwise) and are given in UTC (Universal Time Coordinated).

2 The models

2.1 Geographic and oceanographic setting

The Baltic Sea is a semi-enclosed marginal shelf sea with a mean water depth of 55 m and with narrow shallow connections to the North Sea. Due to river runoff, the water balance is positive driving an estuarine circulation with quasi-permanent outflow of fresh surface waters and an intermittent inflow of salty water from the North Sea. At the surface, this creates a horizontal salinity gradient with high salinities in the west and almost freshwater conditions in the far north. Salinity is increasing with depth thus stratifying the water column year-round and generating a permanent halocline at about 60-m depth in the deeper basins. For more details see Feistel et al. (2008), Leppäranta and Myrberg (2009), or Osínski et al. (2010).

The survey area of the “Expedition Clockwork Ocean” was located in the western Baltic, to the south of the island of Bornholm (Fig. 1). This region is separated into two basins, the Arkona Basin and the Bornholm Basin. The Arkona Basin is the smaller one with a maximum water depth of 51 m, while the maximum depth of the Bornholm Basin is 92 m. The basins



are connected by two channels, with an exchange of water limited by sills of 45 m depth in the Bornholmsgat (Magaard and Rheinheimer, 1974) and 31 m between Rönnebank and the island of Rügen.

2.2 HBM

HBM (HIROMB-BOOS model (Berg, 2012)) is an operational ocean circulation model providing forecasts of the physical conditions in the Baltic Sea. The horizontal resolution is about 1 nm (nautical mile). In the vertical direction, the model domain is separated into 25 depth levels, spaced at 5 m between the sea surface and 100-m depth, and additional levels below at 150, 200, 300, and 400-m depth. The HBM forecasts are available at CMEMS (Copernicus Marine Environment Monitoring Service, <http://marine.copernicus.eu>, product BALTICSEA_ANALYSIS_FORECAST_PHY_003_006, last access 1 March 2019) since 1 April 2015, comprising daily mean and hourly instantaneous fields. For this article, the HBM daily mean fields of June 2016 were utilised.

2.3 ROMS

The employed numerical ocean circulation model ROMS is a hydrostatic, free-surface, primitive equations model. Its algorithms are described in detail in Shchepetkin and McWilliams (2005). In the vertical, the primitive equations are discretised over a variable topography using stretched terrain-following coordinates, so-called s -coordinates (Song and Haidvogel, 1994). In the horizontal, spherical coordinates are used. Biharmonic mixing along isopynic surfaces is applied to the tracers, both in R500 and R100, while biharmonic mixing of momentum is used in R500 and a monoharmonic formulation in R100. The vertical mixing of momentum and tracers is parameterised with the GLS (Generic Length Scale) scheme by Umlauf and Burchard (2003) in R500, and with the interior closure by Large et al. (1994) in R100, referred to as the KPP scheme. For the bottom friction, a quadratic law is applied, and the pressure gradient term is computed using the standard density Jacobian algorithm by Shchepetkin and Williams (2001). The air-sea interaction boundary layer in ROMS is formulated by means of the bulk parameterisation by Fairall et al. (1996). R500 and R100 have the parameters and equations listed in Table 1 in common, while the individual grid-size-dependent parameters and properties are summarised in Table 2. As the spatial scales of the smallest known STPPs are $\mathcal{O}(10\text{ m})$, it is expected that large and medium-scale STPPs are resolved.

2.4 Nesting, boundary conditions

There are two offline nesting steps: R500 is nested in HBM, and R100 is nested in R500. While the ROMS-to-ROMS nesting is technically straightforward, the first nest is somewhat more delicate, because the HBM-output is provided on depth levels while ROMS uses s -coordinates. In addition, the bathymetry of HBM is not contained in the output provided by CMEMS. Therefore, the setup of the R500 domain and the nesting was accomplished as follows:

1. The bathymetry of the GEBCO_2014 grid (General Bathymetric Chart of the Oceans, 30 arc seconds horizontal resolution) was used as the lower boundary of the R500 domain, and it was smoothed iteratively until the stability condition $rx_0 \leq 0.2$ was reached everywhere (see Haidvogel et al. (2000) and Table 2).



2. The HBM prognostic variables were interpolated linearly onto the R500 horizontal grid at each HBM depth level in 24-hour intervals and for each day of June, i.e. from 1 June 00:00 to 30 June 24:00.
 3. The R500 vertical grid was defined according to Table 1 and the HBM fields were interpolated vertically onto the R500 vertical grid. The first cycle of the resulting data set served as initial condition for the R500 integration, while the lateral boundary conditions were extracted from all 31 cycles.
 4. R500 was integrated for one day, and the near bottom velocities were checked for odd features that might have been caused by improper alignment of the R500 bathymetry with the unknown HBM bathymetry. If such features (e.g. abnormal vertical motions) were noticed, the R500 bathymetry was manually adjusted and the above procedure was iteratively repeated, starting with step 3.
- For the R500-to-R100 nesting, the same vertical grid definition was used, and no interpolation from depth levels to s-coordinates was required. Special care was taken for the preparation of the initial and boundary conditions, as a nesting ratio of 5 is rather challenging: the prognostic variables of R500 were interpolated with cubic splines onto the child's grid where the horizontal position of every 5th tracer point in R100 was identical to the position of the corresponding grid point in R500. In addition, the downscaled fields were generated in 3-hour intervals, leading to a smoother temporal change of the lateral boundary conditions. Cubic splines were used as well for the interpolation of the atmospheric forcing fields on the R100 grid. Because in a nested configuration, the s-coordinates of the parent and the child at any location are only identical if the bathymetry is the same, the bathymetry of R100 was cloned from R500 and linearly interpolated onto the finer grid.
- For each nest, radiation boundary conditions with nudging (Marchesiello et al., 2001) were applied to temperature and salinity, barotropic and baroclinic momentum, and the mixing of turbulent kinetic energy along the lateral boundaries. The boundary conditions of the free surface were defined according to Chapman (1985). In all ROMS setups, the nudging time scales were set to 2 days for the corresponding variables. At the surface, the air-sea interaction was specified by means of atmospheric forcing fields from the ICON-EU model, provided by the German Weather Service (DWD). The horizontal resolution of ICON-EU is about 6.5 km and output is produced in 1-hour intervals.

3 R500: model results and validation

- STPPs are generated in the straining field of mesoscale eddies. According to Osínski et al. (2010), the condition for eddy resolving models of the southern Baltic is that the Rossby radius is resolved by at least 4–5 horizontal nodes. As the Rossby radii in the Bornholm and Arkona Basins are in summer around 7.2 and 3.7 km, respectively (Fennel et al., 1991), and since the grid size of HBM is 1 nm, it is definitively not eddy-resolving or even eddy-permitting (2–3 nodes) in the Arkona Basin and perhaps eddy-permitting at best in the Bornholm Basin. The eddy-resolving R500 was initialised from HBM on 1 June 00:00 and integrated for 30 days, thus covering the entire survey period of the “Expedition Clockwork Ocean”. The vertical mixing in R500 is accomplished with GLS using the $k - \omega$ setup of Wilcox (1988) with the stability function of Kantha and Clayson (1994).



Salinity is the ideal parameter to trace turbulent patterns because it is insensitive to the net surface heat flux blurring the surface signal of temperature or density and superimposing a strong seasonal trend, especially in June. Fig. 2 shows salinity in the uppermost layer of HBM and R500 on 1, 10, 20, and 30 June (left and centre panels). R500 rapidly develops turbulent structures that are only marginally identifiable in HBM. These are, for example, the low-salinity outbreaks along the northern boundary visible on 10 and 20 June, a high-salinity eddy in the Arkona Basin, and mushroom-like patterns east and southeast of Bornholm on 1 and 10 June, respectively. The horizontal scales of these features are $\mathcal{O}(10 \text{ km})$, but also smaller patterns with a horizontal extent of 5 km, or even less, are generated by R500, such as the filaments around Bornholm and the meanders immediately off the Polish coast on 20 June. Hence, R500 apparently bridges the gap between the mesoscale and the submesoscale.

R500 provides the initial and boundary conditions for R100. Insofar, it is worth knowing to what extent its generated two-dimensional turbulence is in a state of statistical equilibrium, and at what time during the integration an equilibrium state is attained. The blue dash-dotted graph in Fig. 3 shows a time series of the domain-averaged total kinetic energy, TKE_{R500} ; it fluctuates strongly between 3×10^{-3} and more than $12 \times 10^{-3} \text{ m}^2 \text{ s}^{-2}$ and does not reach a stable value. By contrast, the cumulative average $\overline{TKE_{R500}}$ (red dash-dotted graph) decreases slowly between 1 and 5 June and then increases again to a maximum on 14 June. Evidently, TKE_{R500} is strongly impacted by wind bursts as shown by the black curve. To provide a rough estimate of the spin-up time, R500 was compared to a run where the atmospheric forcing was completely turned off by setting the air-sea fluxes of net heat, fresh water and momentum to zero. This run is referred to as R500_NF (“No Forcing”). Here, the intense fluctuations of TKE vanished as shown by TKE_{R500_NF} (blue solid graph), but there are still some smaller-scale oscillations with maxima on 11, 14, 20, and 28 June exhibiting a slight correlation with the wind bursts lagging behind for about one day. Potentially, these features are triggered by the remote forcing of HBM via the lateral boundaries which explains the time lag. Another cause could be vacillations of TKE which is a well-known peculiarity of nonlinear rotating fluids (Hide, 1958; Früh, 2015). Whatsoever, the cumulative average $\overline{TKE_{R500_NF}}$ attains a maximum of 6×10^{-3} on 1 June and then steadily decreases to about $3.4 \times 10^{-3} \text{ m}^2 \text{ s}^{-2}$ on 7 June. Thereafter, it increases again to 4.4×10^{-3} on 30 June, corresponding to an e-folding scale of 12 days that is in agreement with the progression of the TKE_{R500_NF} graph reaching a quasi-stable value of $4.45 \times 10^{-3} \text{ m}^2 \text{ s}^{-2}$ on 11 June.

An analysis of the prognostic fields of R500_NF yielded an unexpected finding: the tracer fields exhibit much more spatial variability in comparison to the corresponding fields of R500 (see the right panel in Fig. 2). A rich variety of smaller details is revealed that were hidden in the forced run, such as the STPPs along the German and Polish coast, multiple filaments in the entire model domain, and sharper frontal gradients. On longer time scales, the larger scale patterns also develop differently. The authors speculate that the wind field blurs the small-scale features by horizontal mixing as shown by Mahadevan et al. (2010), or that the vertical mixing in the absence of surface fluxes enhances frontal gradients and the fronts become more unstable. This finding is important because it will guide the setup of the R100 experiments below.

A comparison with observations is shown in Fig. 4 by means of the surface salinity from R500 and a RGB composite derived from a satellite-borne multi-spectral image in the visible spectral range. In the latter, the patterns arise due to the presence of naturally occurring optically active substances like chlorophyll, which act like flow tracers. The image reveals three spiral-like



patterns that may be considered as proxies for cyclonic (C1, C2) and anticyclonic (AC) eddies. The centre of C1 is almost at exactly the same location [15°30' E, 54°40' N] in the satellite image and in R500. The centre of C2 is at about [14°10' E, 55°7' N] in R500. Unfortunately, the central part of this cyclone is masked by clouds in the satellite image, but the unmasked portions provide evidence for its real existence. Strong peripheral fronts are visible both in R500 and the satellite images. The positions of AC differ the most: in Fig. 4b, the centre of that anticyclone is at [15°50' E, 54°57' N], in Fig. 4a at about [15°40' E, 55°0' N], hence roughly 7 nm to the west. It is legitimate to associate these positions with each other because both in R500 and in the satellite snapshot, as AC is the anticyclonic “partner” of C1, both form a mushroom-like eddy pair. On the whole, the apparent similarities between the observations and the R500 simulations make the model output trustworthy.

4 R100: results

Apparently, R500 is able to reproduce STPPs but only those in the low-wavenumber part of the spectrum. To provide more insight into the higher-wavenumber parts and to cover the entire period of the “Expedition Clockwork Ocean”, R100 was initialised from R500 on 15 June 00:00 and integrated until 29 June 00:00. Based on the experience with R500, the surface fluxes in R100 were turned off and different formulations and coefficients for the horizontal eddy viscosity and diffusivity were tested. The best results were obtained from a model run with mono-harmonic mixing for the momentum and biharmonic mixing for the tracers (Table 2). This choice caused a minimum damping of STPPs, and a better representation of small-scale details without numerical noise. Moreover, as R100 is rather expensive in terms of computer resources, the vertical mixing was parameterised with KPP instead of the time-consuming GLS scheme. From a *TKE* analysis, the spin-up time was an estimated 2 days. Hence, a 6-day spin-up period starting on 15 June was sufficient to produce statistically equilibrated fields at the beginning of the survey on 20 June.

4.1 Tracer patterns

The top-layer patterns of salinity and potential temperature are shown in the left and centre panels of Fig. 5 in 3-day intervals for the observational period. The top layer ranges between about 0.3 and 1.7 m. To assess the effect of the downscaling, the salinity patterns are compared with the corresponding ones of R500_NF on 20 and 30 June (Fig. 2). The large-scale features resemble each other to a high degree, such as the low salinity to the west and the east of Bornholm and the higher-salinity pool south of the island. However, R100 exhibits much more variability in the submesoscale waveband and STPPs down to 1-km scales are resolved. The signatures of such small-scale features are better visible in the temperature patterns, such as the cold patches in the southern region of the R100 domain.

The knowledge of the temporal change of the density (or buoyancy) gradient is essential for frontogenetic and frontolytic processes and filamentogenesis, that is expressed by the frontal tendency equation (Holton, 1982; Capet et al., 2008b; Gula et al., 2014). As a first approach, the absolute horizontal gradient of potential density, ρ ,

$$|\nabla\rho| = \sqrt{\left(\frac{\partial\rho}{\partial x}\right)^2 + \left(\frac{\partial\rho}{\partial y}\right)^2} \quad (1)$$



is calculated, where x and y are the Cartesian coordinates pointing to the east and to the north, respectively. This quantity is shown in the right column of Fig. 5. Narrow filaments indicate locations of intensified gradients, i.e. density fronts. From the sequence of the images, it appears that the quantity of the fronts increases with time and that the gradients amplify. This is partly confirmed by a frequency distribution of $|\nabla\rho|$ (not shown): from 20 to 26 June, the frequency grows consistently in all frequency intervals. From 26 to 29 June, however, this behaviour changes. While the frequency distribution for $|\nabla\rho| < 0.8 \times 10^{-3} \text{ kg m}^{-4}$ remains almost the same, it decays at the same time for larger values of $|\nabla\rho|$. Hence, there are less locations with strong gradients indicating a weakening of strong density fronts. For the present time, it is open whether there is an upper limit for the growth of $|\nabla\rho|$ and what process delimitates it. Concerning the latter and according to Sullivan and McWilliams (2018) and Gula et al. (2014), who investigated the life cycle of a dense filament, the frontogenesis is arrested at a small width of about 100 m. It is mostly driven by an enhancement of turbulence through submesoscale horizontal shear instabilities that draw their energy primarily from the horizontal mean shear via the horizontal Reynolds stresses.

4.2 Kinematics

Fig. 6 shows the near-surface properties of the velocity field and derived quantities on 26 June. This day was chosen because it represents the conditions in the middle of the survey period and it allows comparisons with Fig. 5.

4.2.1 Horizontal currents

The horizontal velocity field (Fig. 6a) is separated into two regimes: high current speeds frequently exceeding 0.1 m s^{-1} are found north of about $54^\circ 50'$ N, south of $54^\circ 35'$ N, and west of $14^\circ 40'$ E. They are organised in jet-like streaks or circular features, and their positions are clearly related to the main density fronts shown in Fig. 5. Maximum speeds of 0.32 m s^{-1} are found in the anticyclonic eddy southeast of Bornholm. The high-speed regime surrounds a pool of water with speeds lower than 0.1 m s^{-1} in the centre of the model domain. The transition between the high-speed and low-speed regimes appears to be related to the 40-m depth contour (the white line in Fig. 6a), at least in the south and west. Potentially, the bathymetry is acting as a waveguide for the westward jet south of Bornholm.

4.2.2 Relative vorticity

Information about the dynamical properties of the flow field is derived from the relative vorticity ζ , i.e. the vertical component of the curl of the total velocity:

$$\zeta = (\nabla \times \mathbf{V})_z = \frac{\partial v}{\partial x} - \frac{\partial u}{\partial y} \quad (2)$$

Here, z is the vertical coordinate and u, v, w are the zonal, meridional, and vertical components of the total velocity vector \mathbf{V} . Fig. 6b reveals the whole range of relative vorticity (scaled by f) between the largest scales of about 20 km and the smallest scales on the order of the grid size of 100 m. The dominant mesoscale patterns are the large anticyclonic relative vorticity patch southeast of Bornholm and the wavelike structures to the south that belong to the westward jet mentioned above. Further west



and south in the shallow water, pools of concentrated cyclonic relative vorticity vary mostly between 5 and <1 km in size. The smallest visible features are cyclonic streamers, with width approaching the Nyquist scale of 200 m.

There is a strong asymmetry between the distributions of cyclonic and anticyclonic relative vorticity. The cyclonic relative vorticity is organised in thin filaments, comma-like “hooks”, and quasi-circular pools of water. In contrast, the distribution of the anticyclonic relative vorticity is smoother, and the occupied area is larger than the area utilised by $\zeta/f > 0$, which is in agreement with McWilliams (2016). The frequency distribution shows that $\zeta/f < 0$ in 63 % of the grid cells, while positive values are found only in 37 %. Moreover, in less than 0.2 % of the grid cells, $\zeta/f < -1$, indicating negative potential vorticity (Dewar et al., 2015; Gula et al., 2016b) and associated inertial instability.

The relative vorticity structures north of 55° N exhibit lamellar patterns that are probably caused by false advection from the parent domain, although cubic splines were applied to all prognostic variables in the context of the downscaling. Such patterns are only visible in the relative vorticity patterns, while the horizontal velocities (Fig. 6a), and the tracer fields (Fig. 5) look rather reliable. Obviously, the downscaling did a good job with the prognostic variables, but along the open boundaries it may not have been able to reflect the first derivatives correctly.

4.2.3 Divergence and vertical motion, impact of bathymetry

The horizontal divergence of the velocity,

$$\delta = (\nabla \cdot \mathbf{V})_h = \frac{\partial u}{\partial x} + \frac{\partial v}{\partial y} \quad , \quad (3)$$

is displayed in Fig. 6c. It can be divided into 3 different classes of textures: Class I structures are thin, less than 1-km wide filaments of negative divergence (convergent flow) that are bordered by wider areas of divergent flow on one or both sides. The major density fronts (Fig. 7) are aligned with such filaments. On the contrary, the areas of convergent flow that are not congruent with enhanced horizontal density gradients belong to Class II. In particular, those patterns tagged by the yellow arrows in Fig. 7 are not correlated with enhanced density gradients (note that the value of the magenta contour refers already to rather low gradients, cf. Fig. 5). It is conjectured that these features are related to internal waves generated during the genesis of nearby fronts and jets (Shakespeare and Taylor, 2014; Plougonven and Snyder, 2007). This is confirmed by Fig. 8: the vertical displacements of isopycnals between 15°07' E and 15°09' E are clear indicators for internal waves with a wavelength around 1000 m.

Class III textures are small patches of either sign and horizontal scales of $\mathcal{O}(1)$ km. They are found almost everywhere, but their highest values are found in the area of higher current speeds in the northwest corner of the domain and in the anticyclonic eddy southeast of Bornholm. The topography of potential density surfaces in the anticyclone shows that the patches are accompanied by large excursions of isopycnals, indicating intense internal wave activity. These waves are emitted from fronts at the periphery of the eddy, and the superposition of internal waves coming from different directions leads to the rugged shape of isopycnals and contemporaneously to the patchy pattern.

As ROMS is a hydrostatic model, the vertical speed is not computed from the vertical component of the Navier-Stokes equation, but from the continuity equation, instead. As expected, the spatial patterns of the vertical speed are therefore identical



with that of the divergence, but only for the divergence in the top layer and the vertical speed at the base of that layer. In contrast, the horizontal distribution of the vertical speed at 5-m depth (Fig. 6d) still resembles the top layer divergence, but with significant differences. The most striking discrepancy is that the thin filaments of convergent flow belonging to Class (Fig. 6c) are not at all reflected by the vertical motion pattern. On the other hand, the vertical motions related to the internal wave packets discussed above are still clearly visible. To explain this disagreement, Fig. 8 shows a zonal section of the vertical speed, together with the potential density and the meridional velocity. The vertical motion induced by the internal waves attains speeds of up to $\pm 20 \text{ m day}^{-1}$ and the signal is pronounced over the entire vertical range between the surface and 10-m depth; by contrast, the magnitude at the location of the front barely exceeds 5 m day^{-1} and the vertical speed diminishes with increasing depth. Apparently, the major surplus (deficit) of mass created by the frontal convergence (divergence) at the surface, is discharged (imported) by the frontal jet or the secondary divergent circulation (cf. Fig. 1 in McWilliams et al. (2009), or Bleck et al. (1988)). As such a horizontal discharge/import mechanism is not available in a pure internal wave field, the only way to respond to any non-zero divergences is by vertical motion; this is explained in more detail in Section 4.3.4.

In Section 4.2.1, it was already mentioned that the horizontal current patterns are somehow correlated with the water depth. Such a relationship applies as well for the patterns of the other variables displayed in Fig. 6. The spatial variability of relative vorticity and the frequency of narrow filaments of confluent flow are clearly enhanced in the shallow water regions. In contrast, the texture of the vertical speed is rather smooth there, indicating less internal wave activity.

4.3 Fronts and eddies

4.3.1 Frontogenesis and eddy formation

The right column of Fig. 5 shows snapshots of $|\nabla\rho|$. A statistical analysis indicates an increase of the frequency of occurrence of high density gradients and a general sharpening of the density fronts with time. However, the latter provides only a statistical information and it does not show the locations where the fronts are sharpening (frontogenesis) or weakening (frontolysis) and which physical processes are contributing thereto. The missing information is conveyed by the frontal tendency equation

$$F = \frac{d}{dt} |\nabla\rho|^2 \quad , \quad (4)$$

which was introduced by Hoskins (1982) into the meteorological literature. F describes whether the absolute horizontal density gradient of a Lagrangian water parcel is growing ($F > 0$) or weakening ($F < 0$) with time t . Using the nomenclature of Capet et al. (2008b), F is further decomposed as

$$F = (\mathbf{Q}_h + \mathbf{Q}_w + \mathbf{Q}_{dv} + \mathbf{Q}_{dh}) \cdot \nabla\rho \quad . \quad (5)$$

Here, the terms are defined as

$$\mathbf{Q}_h = - \left(\frac{\partial u}{\partial x} \frac{\partial \rho}{\partial x} + \frac{\partial v}{\partial x} \frac{\partial \rho}{\partial y}, \frac{\partial u}{\partial y} \frac{\partial \rho}{\partial x} + \frac{\partial v}{\partial y} \frac{\partial \rho}{\partial y} \right), \quad (6)$$



which is the vector representing the straining deformation by the horizontal total velocity. The vector may be separated into contributions \mathbf{Q}_{geo} from the geostrophic and \mathbf{Q}_{ageo} from the ageostrophic velocity, respectively.

$$\mathbf{Q}_w = -\frac{\partial \rho}{\partial z} \left(\frac{\partial w}{\partial x}, \frac{\partial w}{\partial y} \right) \quad (7)$$

is the equivalent quantity for the vertical velocity, and

$$5 \quad \mathbf{Q}_{dv} = \left(\frac{\partial \rho}{\partial z} \frac{\partial^2 A_V^{\rho}}{\partial x \partial z} + \frac{\partial A_V^{\rho}}{\partial z} \frac{\partial^2 \rho}{\partial x \partial z}, \frac{\partial \rho}{\partial z} \frac{\partial^2 A_V^{\rho}}{\partial y \partial z} + \frac{\partial A_V^{\rho}}{\partial z} \frac{\partial^2 \rho}{\partial y \partial z} \right) \quad (8)$$

is the contribution from vertical mixing where $A_V^{\rho} = A_V^{\rho}(x, y, z, t)$ is the eddy diffusion coefficient for density. Finally,

$$\mathbf{Q}_{dh} = \left(\frac{\partial D}{\partial x}, \frac{\partial D}{\partial y} \right) \quad (9)$$

is the effect of the horizontal diffusion of density, D .

The components of the tendency equation are displayed in Fig. 9 for a subregion of the R100 domain. The quantities F ,
 10 Q_{geo} , Q_{ageo} , Q_w , Q_{dv} , and Q_{dh} at 2-m depth are shown in the centre and bottom rows. They are the scalar products of the
 corresponding vectorial quantities \mathbf{Q} and $\nabla \rho$. For comparison with the dynamical background, the top-layer patterns of $|\nabla \rho|$,
 ζ/f , and the vertical velocity w at 5-m depth are displayed in the top row of the same figure. The subplots of $|\nabla \rho|$ and ζ/f
 reveal four major frontal systems, F1–F4, and two cyclonic vortices, C3 and C4. The width of all fronts and the radius of the
 circular cyclone C3 (defined by the zero-crossings of ζ/f) is ≤ 2 km, while the semi-axes of the elliptical-shaped cyclone C4
 15 vary between 2 and about 4 km. Both frontogenetic and frontolytic processes are roughly evenly distributed and of the same
 order of magnitude for F , Q_{geo} , and Q_w . This is different for Q_{ageo} and Q_{dv} which are primarily frontogenetic. Moreover,
 Q_{dv} only differs significantly from zero at the fronts, while at the positions of C3 and C4, it is close to zero. By contrast, the
 contribution of Q_{dh} to the tendency F is everywhere negligible. F exhibits a bimodal pattern for F1 and F2, with $F < 0$ on the
 anticyclonically sheared side and $F > 0$ on the cyclonic side. A comparison of the patterns of the components of F reveals that
 20 $F > 0$ in F1 and in the western and central parts of F2 is predominantly supported by Q_{ageo} and Q_{dv} and to a lesser extent by
 Q_{geo} , while the sign of Q_w is alternating along-front. On the other hand, $F < 0$ in those parts is primarily supported both by
 $Q_{geo} < 0$ and $Q_{dv} < 0$. A bimodal structure is also visible for F4. Here, frontogenesis is supported both by Q_{geo} and Q_{ageo} ,
 and frontolysis only by Q_w . For F3, the situation is similar.

The above results conflict to those obtained by Capet et al. (2008b), referred to as CMMS in the following: according to their
 25 Fig. 7, the “residual” (equivalent to F in this paper) at the sea surface is generally negative and the geostrophic contribution is
 always positive, while the corresponding quantities in the current article exhibit a clear bimodal structure. On the other hand, the
 contributions from ageostrophic straining and vertical diffusion are bimodal in CMMS but Q_{ageo} and Q_{dv} are predominantly
 positive. Similarly, the impact from vertical straining in CMMS is everywhere negative, in contrast to Q_w that is bimodal as
 well and the sign is alternating along-front. The cause for these disagreements might be the different horizontal resolution of
 30 ROMS (750 m in CMMS and 100 m in R100). By contrast, F and its components resemble more those obtained by Gula et al.
 (2014): these are the bimodal (or even three-modal with filaments) structures and the alternating along-front sign changes.

Prominent structures of the tendency terms are also visible in C3 and C4, but those will be investigated in detail in a follow-up
 paper investigating the dynamics of a submesoscale cyclone.



4.3.2 Submesoscale upwelling in eddies

As noticed above, the vertical motion pattern in almost the entire model domain is impacted by internal waves that frequently blur the corresponding signals of STPPs. However, in some settings, the vertical motion related to submesoscale fronts and eddies may supersede the internal wave-driven vertical velocity which can be seen in Fig. 6d. Such a situation is given during the life cycle of the submesoscale eddy C3 depicted in Fig. 9. C3 originates from a dense (cold and salty) streamer that invaded the area from the south, starting on 24 June around noon. While the streamer stretched farther to the north, it rolled up into C3 on 25 and 26 June (Fig. 10a–c; the entire process is shown in an animation on the web site https://www.hzg.de/institutes_platforms/coastal_research/operational_systems/coast_ocean_measurement/topics/index.php.de#tab-100, last access 1 March 2019). In Fig. 10d–f, the vertical speed at 5-m depth is shown for the same period of time. On 24 June before the winding-up of the eddy started, the vertical motion pattern is controlled by a train of internal waves travelling from northeast to southwest. One day later, the impact of the eddy formation on the vertical motion field becomes visible: two extended patches with vertical speeds of either sign are located south and north of the eddy core. On 26 June, the pronounced downwelling area is smaller but the upwelling still prevails at the same location. Apparently, the eddy-driven vertical motion supersedes the signal of the internal waves and causes persistent upwelling for a day or even more as can be seen in Fig. 10f: at the position of the crosshair, upwelling is still visible, although the eddy centre has moved already to the north by about 2 nm.

4.3.3 Instability mechanisms

The results above impressively show that submesoscale eddies grow rapidly in the R100 domain, preferably in the shallow areas with water depths less than 40 m (Fig. 6). However, it is not yet clear if inertial, symmetric or mixed-layer instability drive the eddy growth. In the following, the R100 fields are analysed for criteria necessary for the occurrence of any type of these instabilities.

For inertial instability, negative absolute vorticity, ζ^a , is a necessary condition, which is equivalent to $\zeta^a = \zeta + f < 0$ or $\zeta/f < -1$. It can be seen in Fig. 6b (blue regions) that $\zeta/f < -1$ is satisfied along the coast of Bornholm and at a few isolated locations along the meridional open boundaries, i.e. close to the centre of the cyclonic eddy in the northwest corner and between $54^\circ 25'$ and $54^\circ 30'$ N at the eastern boundary. However, the latter appearances are ignored because they are potentially due to false advection effects of relative vorticity discussed above. A zoomed image of ζ^a/f in the surface layer of R100 (Fig. 11) shows that negative values are found at 7 locations around Bornholm, indicating the birthplaces of disturbances driven by inertial instability. All of them are directly attached to the coast, but favourable conditions for the growth of the disturbances seem to prevail only at sites no. 2 and 5 (yellow circles). In detail, on 26 June negative absolute vorticity is visible at no. 2, 3, 5, and 7. But within the subsequent 3 days, anticyclonic eddies have only developed at sites no. 2 and 5. It is common to these sites that the coast is on the right, relative to the current direction, and that the relative vorticity is anticyclonic due to the no-slip condition at the lateral solid boundaries. However, at sites no. 2 and 5, the curvature of the coastline is anticyclonic in contrast to the other sites. Apparently, a solid boundary on the right and anticyclonic curvature of that boundary, are additional necessary conditions for the formation of eddies driven by inertial instability. These conditions are also satisfied at



site no. 7, but there is no indication for eddy growth. It is most likely prevented by the southward current with cyclonic vorticity along the west coast of the island. The above findings are in agreement with Gula et al. (2016b) who showed that equivalent conditions were satisfied in the Gulf Stream where the anticyclonic shear is amplified by the topographic drag against the slopes of the Great and Little Bahama Banks on its way through the Florida Straits. A similar situation is given where the California Undercurrent passes along Point Sur Ridge, a topographic obstacle near Monterey Bay (Dewar et al., 2015; Molemaker et al., 2015). Both cases lead to the formation of unstable submesoscale fronts and eddies.

According to Thomas et al. (2013), symmetric instability occurs when

$$\phi_{Ri_{geo}} < \phi_c \quad , \quad (10)$$

with

$$10 \quad \phi_{Ri_{geo}} = \tan^{-1} \left(-\frac{1}{Ri_{geo}} \right) \quad (11)$$

and

$$\phi_c = \tan^{-1} \left(-\frac{\zeta_{geo}^a}{f} \right) \quad . \quad (12)$$

Here,

$$Ri_{geo} = \frac{f^2 N^2}{|\nabla_h b|^2} \quad (13)$$

15 is the Richardson number of the geostrophic flow,

$$b = -\frac{g\rho}{\rho_0} \quad (14)$$

is the buoyancy,

$$N^2 = -\frac{g}{\rho_0} \frac{\partial \rho}{\partial z} \quad (15)$$

the squared Brunt-Väisälä frequency, and

$$20 \quad \zeta_{geo}^a = f + \frac{\partial v_{geo}}{\partial x} - \frac{\partial u_{geo}}{\partial y} \quad (16)$$

the absolute vorticity of the geostrophic flow $\mathbf{V}_{geo} = (u_{geo}, v_{geo})$. ρ_0 is a constant reference density, and g the gravitational acceleration. Specifically, in regions where $\zeta_{geo}^a/f > 1$ (cyclonic vorticity), symmetric instability prevails, if the conditions

$$C_{SI} = -90^\circ < \phi_{Ri_{geo}} < \phi_c \quad \wedge \quad \phi_c < -45^\circ \quad (17)$$

are satisfied. By contrast, symmetric instability is the dominant mode of instability in regions of anticyclonic vorticity ($\zeta_{geo}^a/f < 1$), if

$$C_{SI} = -90^\circ < \phi_{Ri_{geo}} < -45^\circ \quad \wedge \quad \phi_c > -45^\circ \quad . \quad (18)$$



As the condition described by eq. (10) must be satisfied in the mixed layer for symmetric instability to occur, all above quantities were evaluated in R100 at 3-m depth. Note that the relative vorticity is identical to the relative vorticity of the geostrophic flow, because ζ is the curl of the rotational, divergence-free part of the total velocity which is the geostrophic velocity by definition. Hence, a decomposition of the total velocity in a geostrophic part \mathbf{V}_{geo} and an ageostrophic part \mathbf{V}_{ageo} requiring a Poisson solver is redundant (for some test cases, both ζ_{geo} and ζ were evaluated showing identical results). For simplification, the subscript “geo” will therefore be dropped for ζ_{geo}^a and Ri_{geo} . Fig. 12 shows ϕ_{Ri} , ϕ_c , and C_{SI} at the start of the model integration on 15 June (using as initial condition when the corresponding field is mapped from R500 on the 100-m grid), and on 26 June. On 15 June, there are large areas where $-90^\circ < \phi_{Ri} < -45^\circ$ (Fig. 12a, in blue), indicating satisfaction of the first condition of eqs. (17) and (18). However, this condition is only necessary and sufficient for regions of cyclonic vorticity ($\phi_c < -45^\circ$). Considering the second condition in eq. (18), necessary and sufficient conditions for regions of anticyclonic vorticity are satisfied, if, and only if, $\phi_c > -45^\circ$. Linking the requirements for ϕ_c (Fig. 12c) and ϕ_{Ri} yields the logical map Fig. 12e for 15 June, indicating where eqs. (17) and (18) are satisfied for cyclonic and anticyclonic vorticity, respectively. Compared to the fairly widespread areas where the necessary conditions for ϕ_{Ri} and ϕ_c are met separately, the necessary and sufficient conditions for C_{SI} are satisfied only in rather limited streaks. Nine days later, on 26 June, there are just a few spots where even C_{SI} is satisfied (Fig. 12f). Hence, favourable conditions for symmetric instability prevail only during the initial phase of the model integration, becoming less frequent thereafter. More insight into the temporal evolution of the statistics of C_{SI} is provided by the relative frequency of occurrence, $p(C_{SI}) = 100 \cdot n(C_{SI} \equiv true)/N$, where n is the number of grid cells where the criterion for C_{SI} is met, and N is the total number of grid cells. $p(C_{SI})$ decays from 4.8 % on 15 June to 1.8 % on 16 June, which yields an e-folding scale of ≈ 1 day comparable to the inertial period of 14.6 h at this latitude. Thereafter, $p(C_{SI})$ decreases almost steadily and stabilises around 0.5 %. Hence, as symmetric instability extracts kinetic energy from the geostrophic flow at a rate given by the geostrophic shear production (Thomas et al., 2013), this process comes rapidly due to a halt after about one inertial period and mixed-layer instability, presumably, takes over.

Mixed-layer instability is an efficient mechanism to restratify the mixed layer (Boccaletti et al., 2007). For the determination of the mixed-layer depth, MLD, a $\Delta\sigma_\theta = 0.1 \text{ kg m}^{-3}$ -criterion was used, i.e. MLD was defined as the depth where the potential density exceeds the surface density for the first time by $\Delta\sigma_\theta$. The domain-wide mean MLD decreases almost linearly from 12.7 m on 15 June to 5.1 m on 29 June. Hence, the mixed-layer is restratified, probably by mixed-layer instability. In order to exclude that symmetric instability drives the restratification, the relative frequency $p(Ri) = 100 \cdot n(Ri < 1)/N$ was computed. This quantity drops from 23.2 to 4.0 % within the first day of the integration and decreases thereafter slowly to 1.4 % on 29 June. Hence, after about one inertial period, $Ri \geq 1$ almost everywhere, which makes symmetric instability unlikely. This is in accordance with Haine and Marshall (1998) who state that “symmetric instability rapidly generates a layer with vanishing potential vorticity ($Ri = 1$), but non-zero vertical stratification. Thereafter a nonhydrostatic baroclinic instability develops ...”.

4.3.4 Frontal circulation

In order to provide details of the secondary circulation in submesoscale fronts in a non-idealised model, features resembling the confluence situation as provided by a deformation field were identified in the R100 fields of 26 June in the red box indicated in



Fig. 6d. Here, dense water in the east and light water in the west, form a confluent flow pattern and generate a density contrast at the surface of more than 0.4 kg m^{-3} over a horizontal distance of about 2 km within the black rectangle shown in Fig. 13.

Detailed maps of various quantities within that rectangle are displayed in Fig. 14a–e, and vertical cross sections along the dashed lines are shown in Fig. 14f–j. In the western part of the front, the total velocity vectors at the surface are aligned almost parallel to the isopycnals (panel a); extreme values of $|\mathbf{V}|$ are close to 12 cm s^{-1} at the surface. In the cross section (panel f), the v component attains minimum values of $< -10 \text{ cm s}^{-1}$, located by a few hundred metres to the west of the maximum horizontal density gradient (panel b). The velocity field depicts the classical picture of a frontal jet, with a width of about 3 km and the depth around 4 m. It is defined by the -5 cm s^{-1} isotach of the v -component. The horizontal shear of the jet creates a front-parallel band of strong cyclonic relative vorticity with maximum values of $> 1.6f$ (panels c, h). The cross-front width of the band is about 600 m, and the highest values of the relative vorticity are congruent with the maximum horizontal density gradient (panel b). A wide band of anticyclonic relative vorticity extends to the west of the cyclonic region. East of the cyclonic region, several bands with alternating sign are aligned. Vectors of \mathbf{V}_{geo} are superimposed in panel c. A comparison with panels a and c reveals, that the directions of \mathbf{V} and \mathbf{V}_{geo} resemble closely each other in appearance, but the speeds are slightly different. While the maximum speeds of \mathbf{V} are around 12 cm s^{-1} in the jet, those of \mathbf{V}_{geo} are close to 10 cm s^{-1} i.e. the jet is super-geostrophic (Persson, 2001). This is confirmed by panel d which shows the horizontal divergence δ/f , together with the vectors of the ageostrophic flow \mathbf{V}_{ageo} : the meridional components of \mathbf{V}_{ageo} and \mathbf{V}_{geo} have the same (negative) sign, hence \mathbf{V}_{ageo} amplifies the geostrophic jet. The maximum ageostrophic speeds are around 6 cm s^{-1} . In the cross-frontal direction (panel a), the 5.25 kg m^{-3} isopycnal separates two regimes of opposite zonal component of the ageostrophic flow, u_{ageo} : in the lighter water, $u_{ageo} > 0$, and $u_{ageo} < 0$ in the heavier water. While the overall magnitude of u_{ageo} is just a few mm s^{-1} , it attains its highest value of about 1 cm s^{-1} right at the location of the surface outcrop of the 5.25 kg m^{-3} -isopycnal.

The impact of \mathbf{V}_{ageo} on the divergence δ and on the vertical speed w is illustrated in Figs. 14d, i, e, and j. According to panels d and i, extreme values of $\delta/f \approx 0.3$ and $\delta/f \approx -0.8$ are found at the sea surface immediately to the west and to the east of the maximum horizontal density gradient, respectively. The minimum of the divergence (=maximal convergence) drives a deep-reaching downwelling cell with extreme speeds of almost 15 m day^{-1} . Less intense upwelling of maximal $\approx 6 \text{ m day}^{-1}$ is associated with the divergence maximum (panel j). The positions of the extrema of δ/f are also reflected by its horizontal surface distribution in panel d, while a comparison of panels d and e reveals a clear correlation between δ and w . Patches of convergent motion are found also along the 5.25 kg m^{-3} isopycnal in panel i; potentially, they feed the large downwelling area underneath it. Further cells of intense vertical motion are found west and east of the surface front as shown in panel j. Apparently, these patterns are not parts of the secondary circulation, but rather caused by internal waves (see Section 4.2.3) or by another weak front located about 600 m further east.

Overall, the described secondary circulation pattern closely resembles the ones of the idealised model studies mentioned in the Introduction; primarily, this is a “single overturning cell with upwelling and surface divergence on the light side and downwelling and surface convergence on the dense side” (literally after McWilliams (2016)). However, Fig. 14 provides additional details which were potentially not yet highlighted before:



- The frontal jet is super-geostrophic, i.e. the jet speed is amplified by an ageostrophic component. Under the assumption that the jet was in geostrophic balance, the theoretical inclination of the front was calculated as 0.003° using the Margules equation (Margules, 1906), the geostrophic jet speed, and the cross-front density difference. Assuming the $\sigma_\theta = 5.25 \text{ kg m}^{-3}$ -isopycnal as the frontal interface, the tilt angle of that isopycnal was, however, only 0.001° . Hence, the slope of the front is not in geostrophic balance with the jet. This circumstance was not considered in the previous literature, assuming two-dimensionality (Bleck et al., 1988), or quasi-geostrophic (Nagai et al., 2006), or semi-geostrophic (Thompson, 2000) balance. In contrast, in the model of McWilliams (2017) (see Fig. 5 there), the ageostrophic contribution to the jet speed amounts to about 3 cm s^{-1} while the geostrophic fraction is close to 12 cm s^{-1} .
- The maximum speed of the cross-frontal ageostrophic velocity is weaker than expected from earlier models. Right at the surface, it is only 1 cm s^{-1} , while Bleck et al. (1988) arrived at $> 4.5 \text{ cm s}^{-1}$ and McWilliams (2017) at least at 2 cm s^{-1} . A potential reason for this discrepancy is that the other studies did not consider the ageostrophic velocity as being the ageostrophic part of the total flow, but rather as the departure from the (barotropic) deformation velocity or from the far-field average, instead. In the present situation, it was not possible to separate the total flow into such components because they were not defined. Hence, one may speculate that something like the deformation velocity is opposed to the cross-front ageostrophic velocity and attenuates it.
- According to Fig. 14g, the cross-frontal velocity is positive (eastward) in the light water ($\sigma_\theta < 5.25 \text{ kg m}^{-3}$) and westward in the denser water below. Thus, the velocity converges at that isopycnal, in accordance with Fig. 14i. It is not known to the authors whether such a “sloping convergence” was mentioned before in the oceanographic literature.

The investigated front satisfies the criteria to be denoted as “submesoscale”. The first criterion, $Ro \sim \mathcal{O}(1)$, is confirmed by Figs. 14c and h, indicating that the f -scaled relative vorticity (which is equivalent to a local Rossby number) is $\mathcal{O}(1)$. Another criterion is $Ri \sim \mathcal{O}(1)$ (Thomas et al., 2008; Mahadevan, 2016). Therefore, Ri was evaluated in the frontal region, and it reaches $Ri \approx 1.5$ in the frontal region at the location of maximum convergence at the sea surface.

5 Comparison of features with observations

The R100 results presented above have provided a detailed insight into STPPs, such as tracer patterns, kinematic structures, and dynamical processes related to fronts and eddies. A comparison with observations, however, is rather limited because STPPs are difficult to measure due to their small spatial and temporal scales. Namely, in the literature there is an abundance of investigations providing evidence for STPPs, but the information is frequently fragmented because the corresponding experiments were not dedicated explicitly to their exploration.

Observations of STTPs covering a large area originate predominantly from spaceborne or airborne platforms, and they are mostly limited to measurements of the reflected and/or emitted radiance in the visible and infrared part of the spectrum. A spectacular satellite image of a phytoplankton bloom (Fig. 15, courtesy of NASA, National Aeronautics and Space Administration) exhibits the submesoscale spatial variability in the Baltic Proper. The shortest wavelength of meanders driven by



hydrodynamical instability is around 1 km, the width of filaments is $\mathcal{O}(100)$ m, and the diameters of the cyclonic eddies in the southwest and northeast are about 5 and 30 km, respectively. The scales in this image are similar to the R100 results; the comparison is legitimate because the Rossby radius in this area is 5.7 km in summer (Fennel et al., 1991), which is close to the corresponding radii in the Arkona and Bornholm Basins (see Section 3). Note also the fringe-like features along several
5 fronts with wavelengths and amplitudes < 100 m. As all fringe point to the same direction, it is unlikely that they are generated by any type of hydrodynamical instability. Moreover, it is supposed that they are created by the interaction of surface gravity waves and Langmuir cells with fronts (Nobuhiro Suzuki, personal communication, 2018). Similar fringe also become visible in the ocean fronts of Suzuki et al. (2016) (see Figure 2b there), when cross-front winds are directed from the less-dense side of the front to the denser side. Extremely high-resolution images obtained from other aerial observations reveal that even
10 smaller-scale eddies exist.

The complete life cycle of a submesoscale cyclonic eddy with a diameter of ≈ 300 m was observed during the “Expedition Clockwork Ocean” in the southwestern part of the Bornholm Basin. The formation of the eddy started in the morning and it decayed in the afternoon of the same day, hence the lifetime was just a few hours. Peculiar features of this cyclone are spots of cold water (marked as “S” in Fig. 16) near its tail with diameters of about 10 m and mean distances of 20 m. From a video, it
15 appears that the spots are accompanied by breaking surface waves. Potentially, the spots are created by intense turbulent mixing (Marmorino et al., 2013). Because of the small scales it is certainly not possible to model the spots with R100, but it is weird that the model on the one hand reproduces filaments with width of 2 times the model resolution (200 m), and contrariwise, the smallest eddy sizes in R100 are around 1 km, i.e. 10 times the resolution. The same ratio was also observed in R500 where the minimum resolved eddy size was around 5 km. Hence, in order to reproduce eddies like the one shown in Fig. 16 requires
20 further downscaling to a few tens of meters.

A closeup infrared image of another eddy observed in the Southern California Bight is shown in Fig. 17, together with corresponding properties from the modelled cyclone C3 (see Figs. 9, 10). The observed sea surface temperature (panel a) exhibits a spiraliform cyclonic eddy with a diameter of about 1 km, where the diameter is estimated as the width between the ≈ 13.8 °C isotherms (purple) on either side. Special features are the low temperature patches (black) close to the eddy centre
25 suggesting upwelling, and the bright ripples in the southwest which are probably caused by internal waves. One may note also the cold spots “S” along the periphery; they resemble closely those observed in Fig. 16, and they are definitely not caused by a malfunction of the camera, because they show up at different positions in a sequence of images taken within a period of about 20 minutes (see also Figure 2 in Marmorino et al. (2018)). For comparison with C3, the salinity at 15 m depth is provided in panel b. This depth was selected as the mixed-layer depth at the corresponding position in R100 is about 9 m and the surface
30 signal of C3 is hardly resolved (cf. potential temperature and salinity on 26 June in Fig. 5). Moreover, salinity was chosen for comparison because it is the primary component controlling the stratification in the Baltic Sea. The overall structures of the C3 salinity and the sea surface temperature of the observed eddy are looking similar but the smaller details visible in the latter are not reproduced by C3: these are the ripples in the southwest, the cold spots, and as well the texture of the tracer field in the core. Most probably, this is due to the insufficient horizontal resolution of R100 or non-hydrostatic effects which are not
35 included in the applied ROMS version.



Kinematic quantities of STPPS were obtained from direct measurements in the framework of the LatMix and SubEx experiments. Shcherbina et al. (2013) presented a detailed view of submesoscale vorticity, divergence, and strain statistics from synchronous two-ship ADCP (Acoustic Doppler Current Profiler) samplings. Specifically, their observations indicated flows with $Ro \sim \mathcal{O}(1)$ and an asymmetry in the distribution of the relative vorticity skewed towards positive values. The latter is in excellent agreement with the R100 results. By contrast, Ohlmann et al. (2017) identified STTPS with aerial guidance and seeded them with drifters. The Lagrangian observations exhibited high values of relative vorticity and divergence exceeding $5f$, suggesting vertical velocities up to 240 m day^{-1} . Such values are rather close to the values obtained from R100. Similar values for ζ/f and δ/f resulted also from the high-frequency radar observations of Parks et al. (2009). As the observations mentioned above are two-dimensional and confined to the sea surface, they provide only limited information of subsurface properties of STPPs. Somewhat more detailed insight is gained from the high-resolution in-situ measurements of Zhong et al. (2017) which exhibit submesoscale kinematic structures along a vertical section through a 200 km wide mesoscale eddy in the South China Sea. Unfortunately, that eddy is an anticyclone and a comparison with the corresponding quantities in C3 is problematic.

Comprehensive observations of the frontal circulation (Pollard and Regier, 1992; Rudnick, 1996; Pallàs-Sanz et al., 2010) confirm the secondary circulation pattern as predicted from theoretical considerations and numerical models. However, the above studies did not resolve STTPs and the extrema of the vertical velocity are correspondingly low with $\mathcal{O}(10 \text{ m day}^{-1})$. Namely, the vertical velocities in the front shown in Fig. 14e and j are on the same order but this is due to the low water depth. On the contrary, the higher-resolution observations of a submesoscale front oriented along the periphery of a mesoscale eddy (Adams et al., 2017) confirm vertical velocities of $\mathcal{O}(100 \text{ m day}^{-1})$. Moreover, it was demonstrated that within the same front existed confluent and diffluent regions of the cross-frontal velocity. This does not necessarily prove that the ageostrophic velocity changes sign, but it indicates that the generally accepted picture of the secondary circulation is only valid in the case of frontogenesis driven by an externally imposed deformation field.

The formation of a submesoscale cyclonic eddy (Fig. 10) resembles closely the sequence of infrared images published by Munk et al. (2000) (see Fig. 12 there) and the snapshot of Buckingham et al. (2017). In both cases, the eddies originate from an unstable thermal front which finally breaks up in a train of cyclonic eddies. While the diameters of the eddies shown by Munk et al. (2000) are around 10 km (very rough visual estimate), those of Buckingham et al. (2017) are smaller (1–10 km according to the authors).

There are two observational studies available regarding necessary instability criteria at fronts (Thomas et al., 2013; Zhong et al., 2017) but they are not comparable to the maps in Fig. 12 because the criteria were computed along vertical sections across the Gulf Stream front and in a large anticyclonic eddy in the South China Sea, respectively. Concerning frontogenetic or frontolytic processes, computations or estimations of the components of the frontal tendency equation from observational data are not known to the authors.



6 Conclusions

A double one-way nesting approach is used in order to simulate submesoscale turbulent patterns and processes (STPPs) in the southern Baltic Sea in summer 2016. In order to reproduce the mesoscale environment in a realistic way, the Regional Ocean Modeling System (ROMS) with 500-m horizontal resolution (R500) is nested in an existing operational model, and further
5 downscaling to a grid size of 100 m (R100) enables the generation of STPPs. In R500, the kinematic and dynamical structures are rather sensitive to the surface boundary conditions. While the response of mesoscale patterns to the turning-off of the atmospheric forcing is rather sluggish, it has an immediate impact on the generation of smaller-scale features which represent already the low-wavenumber part of submesoscale turbulence in the spectral range between about 1 and 5 km. Consequently, as R100 is intended to enable the generation of STPPs and to analyse their kinematic and dynamical properties without disturbing
10 effects, the atmospheric forcing is turned-off from the outset.

After initialisation, the horizontal buoyancy gradients in R100 grow for about 11 days, and afterwards the frequency of strong gradients begins to decline indicating frontal arrest. STPPs develop rapidly within about a day; they are characterised by relative vorticities and divergences reaching multiple of the Coriolis parameter, and strong vertical speeds of $\mathcal{O}(100)$ m day⁻¹. The frequency distribution of relative vorticity is clearly biased towards negative (anticyclonic) values. The horizontal
15 divergence and the vertical motion are predominantly controlled by the velocity field associated with internal waves and to a lesser extent by frontal secondary circulations.

Typical elements of the secondary circulation of two-dimensional strain-induced frontogenesis are identified at an exemplary front in shallow water; these are the frontal jet, the downwelling on the dense side and upwelling on the less dense side. In addition to the results of idealised two-dimensional models, details of the ageostrophic current field and the related divergence
20 are revealed: the frontal jet is not in geostrophic balance but super-geostrophic, instead. Further on, it is shown that a region of enhanced convergent flow is aligned with the slope of the frontal surface.

The components of the tendency equation are evaluated in a subregion of the R100 domain. At fronts, frontogenetic and frontolytic processes represented by the frontogenetic tendency, F , and the contributions from the straining deformation of the geostrophic and vertical velocity, Q_{geo} and Q_w , respectively, are equipartioned, bimodal, and of the same order of magnitude.
25 By contrast, the contributions from the ageostrophic velocity, Q_{ageo} , and from vertical mixing, Q_{dv} , act primarily frontogenetic while the contribution from horizontal mixing, Q_{dh} , is negligible everywhere.

The conditions for two types of hydrodynamic instability are evaluated for the whole R100 domain: favourable conditions for inertial (centrifugal) instability are found only along coastlines. There, anticyclonic eddies develop rapidly from along-coast currents if the coast is on the right hand side (looking downstream) and if the coastline is anticyclonically curved. During the
30 first day of the R100 integration, symmetric instability is likely to occur in about 5 % of the model domain but within two days, the probability drops to <1 %. Parallel to the rapidly decreasing probability increases the geostrophic Richardson number Ri_{geo} . While at the beginning of the integration, $Ri_{geo} < 1$ in about 24 % of the R100 domain, this number decreases to about 4 % after one day, indicating that mixed-layer instability is the main process depleting the reservoir of potential energy.



While anticyclonic eddies are generated solely along coastlines due to inertial instability, cyclonic eddies are found in the entire R100 domain, but preferably in those regions where the water depth is less than about 40 m. A special feature of the cyclones is their ability to absorb internal waves and to sustain patches of continuous upwelling for several days favouring plankton growth. By contrast to mesoscale cyclones which pinch off from basin-scale fronts, submesoscale cyclones are rolled-up streamers, similar to those observed by Klymak et al. (2016) on the north wall of the Gulf Stream. Hence, it may not be appropriate to denote these features “eddies” but “spirals” instead, as suggested by Munk et al. (2000).

A peculiar feature of the observed eddies shown in Figs. 16 and 17a are the cold spots along their periphery. It is conjectured that the spots are small upwelling cells driven by another unknown mode of instability which links the submesoscale with the microscale and finally leads to three-dimensional energy dissipation. As it is extremely challenging to observe such features with in situ methods, attempts will be made to catch these spots with further downscaling to the $\mathcal{O}(1)$ m scale using non-hydrostatic models or Large Eddy Simulations. These numerical approaches would also serve to explore structures and processes in the interior of eddies in greater detail.

Code and data availability. The model code and the output of the ROMS runs presented in this article are available from the first author on request.

Author contributions. Reiner Onken implemented the double-nested ROMS model for the given region in the Baltic Sea and conducted the model runs. Ingrid M. Angel-Benavides and Burkard Baschek contributed the results from the SubEx experiment in the Southern California Counter Current, and Burkard Baschek coordinated the “Expedition Clockwork Ocean” and the corresponding modeling activities.

Competing interests. The authors declare that they have no conflicts of interest.

Acknowledgements. We thank Rüdiger Röttgers and Hajo Krasemann for the processing of Figs. 4b and 16, and Rainer Feistel who provided details of the Arkona and Bornholm Basins to us. Geoffrey Smith and George Marmorino, Naval Research Laboratory, provided infrared observations taken during the Submesoscale Experiments for comparison. The ICON-EU output was made available by the Thomas Bruns of the German Weather Service (DWD). The output of the HIROMB-BOOS model was downloaded from the Copernicus Marine Environment Monitoring Service, and the bathymetry data from the General Bathymetric Chart of the Oceans were provided by the British Oceanographic Data Centre. The coastline data were obtained from NOAA (National Oceanic and Atmospheric Administration).



References

- Adams, K. A., Hosegood, P., Taylor, J. R., Sallée, J. B., Bachman, S., Torres, R., and Stamper, M.: Frontal circulation and submesoscale variability during the formation of a Southern Ocean mesoscale eddy. *Journal of Physical Oceanography*, 47, 1737–1753, doi: 10.1175/JPO-D-16-0266.1, 2017.
- 5 Berg, P. Mixing in HBM. DMI Scientific Report, 12-03, Danmarks Meteorologiske Institut, København, Denmark, 2012.
- Bleck, R., Onken, R., and Woods, J. D.: A two-dimensional model of mesoscale frontogenesis in the ocean. *Quarterly Journal of the Royal Meteorological Society*, 114, 347–371, 1988.
- Blumen, N.: On short-wave baroclinic instability. *Journal of Atmospheric Sciences*, 36, 1925–1933, 1979.
- Boccaletti, G., Ferrari, R., and Fox-Kemper, B.: Mixed layer instabilities and restratification. *Journal of Physical Oceanography*, 37, 2228–
10 2250, doi: 10.1175/JPO3101.1, 2007.
- Buckingham, C. E., Khaleel, Z., Lazar, A., Martin, A. P., Allen, J. T., Naveira Garabato, A. C., Thompson, A. F., and Vic, C.: Testing Munk’s hypothesis for submesoscale eddy generation using observations in the North Atlantic. *Journal of Geophysical Research Oceans*, 122, 6725–6745, doi: 10.1002/2017JC012910, 2017.
- Charney, J. G.: Geostrophic turbulence. *Journal of Atmospheric Sciences*, 28, 1087–1095, 1971.
- 15 Capet, X., McWilliams, J. C., Molemaker, M. J., and Shchepetkin, A. F.: Mesoscale to submesoscale transition in the California Current system. Part I: flow structure, eddy flux, and observational tests. *Journal of Physical Oceanography*, 38, 29–43, doi: 10.1175/2007JPO3671.1, 2008a.
- Capet, X., McWilliams, J. C., Molemaker, M. J., and Shchepetkin, A. F.: Mesoscale to submesoscale transition in the California Current system. Part II: frontal processes. *Journal of Physical Oceanography*, 38, 44–64, doi: 10.1175/2007JPO3672.1, 2008b.
- 20 Capet, X., McWilliams, J. C., Molemaker, M. J., and Shchepetkin, A. F.: Mesoscale to submesoscale transition in the California Current system. Part III: energy balance and flux. *Journal of Physical Oceanography*, 38, 2256–2269, doi: 10.1175/2008JPO3810.1, 2008c.
- Chapman, D. C.: Numerical treatment of cross-shelf open boundaries in a barotropic coastal ocean model. *Journal of Physical Oceanography*, 15, 1060–1075, 1985.
- Charney, J. P.: The dynamics of long waves in a baroclinic westerly current. *Journal of Meteorology*, 4, 135–163, 1947.
- 25 Dewar, W. K., McWilliams, J. C., and Molemaker, M. J.: Centrifugal instability and mixing in the California Undercurrent. *Journal of Physical Oceanography*, 45, 1224–1241, doi: 10.1175/JPO-D-13-0269.1, 2015.
- Eady, T.: Long waves and cyclone waves. *Tellus*, 1, 33–52, 1949.
- Eliassen, A.: On the vertical circulation in frontal zones. *Geofysiske Publikasjoner* 24, 147–160, 1962.
- Fairall, C. W., Bradley, E. F., Rogers, D. B., Edson, J. B., and Young, G. S.: Bulk parameterization of air-sea fluxes for Tropical Ocean-
30 Global Atmosphere Coupled-Ocean Atmosphere Response Experiment. *Journal of Geophysical Research*, 101, C2, 3747–3764, doi: 10.1029/95JC03205, 1996.
- Feistel, R., Nausch, G., and Wasmund, N. (Eds.): State and Evolution of the Baltic Sea, 1952–2005: A Detailed 50-year Survey of Meteorology and Climate, Physics, Chemistry, Biology, and Marine Environment. Wiley-Interscience, Hoboken, New Jersey, USA, ISBN 978-0-471-97968-5, 2008.
- 35 Fennel, W., Seifert, T., and Kayser, B.: Rossby radii and phase speeds in the Baltic Sea. *Continental Shelf Research*, 11 (1), 23–26, 1991.
- Fox-Kemper, B., and Ferrari, F.: Parameterization of mixed layer eddies. Part I: theory and diagnosis. *Journal of Physical Oceanography*, 38, 1145–1165, doi: 10.1175/2007JPO3792.1, 2008.



- Früh, W.-G.: Amplitude vacillation in baroclinic flows. In: von Larcher, T., and Williams, P. D. (Eds.): *Modelling Atmospheric and Oceanic Flow: Insights from laboratory experiments and numerical simulations*. Wiley, pp. 61–81, doi: 10.1002/9781118856024, 2015.
- Gula, J., Molemaker, M. J., and McWilliams, J. C.: Submesoscale cold filaments in the Gulf Stream. *Journal of Physical Oceanography*, 44, 2617–2643, doi: 10.1175/JPO-D-14-0029.1, 2014.
- 5 Gula, J., Molemaker, M. J., and McWilliams, J. C.: Submesoscale dynamics of a Gulf Stream frontal eddy in the South Atlantic Bight. *Journal of Physical Oceanography*, 46, 305–325, doi: 10.1175/JPO-D-14-0258.1, 2016a.
- Gula, J., Molemaker, M. J., and McWilliams, J. C.: Topographic generation of submesoscale centrifugal instability and energy dissipation. *Nature Communications*, 7:12811, doi: 10.1038/ncomms12811, 2016b.
- Haine, T. W. N., and Marshall, J.: Gravitational, symmetric, and baroclinic instability of the ocean mixed layer. *Journal of Physical Oceanography*, 28, 634–658, 1998.
- 10 Haney, R. L.: On the pressure gradient force over steep topography in sigma coordinate models. *Journal of Physical Oceanography*, 21, 610–619, 1991.
- Haidvogel, D. B., Arango, H. G., Hedström, K., Beckmann, A., Malanotte-Rizzoli, P., and Shchepetkin, A. F.: Model evaluation experiments in the North Atlantic Basin: simulations in nonlinear terrain-following coordinates. *Dynamics of Atmospheres and Oceans*, 32, 239–281, 15 2000.
- Hide, R.: An experimental study of thermal convection in a rotating liquid. *Philosophical Transactions of the Royal Society of London (A)*, 250, 441–478, 1958.
- Holton, J.: The role of gravity induced drag and diffusion in the momentum budget of the mesosphere. *Journal of the Atmospheric Sciences*, 39, 791–79, 1982.
- 20 Holton, J. R.: *An introduction to dynamic meteorology*. Fourth edition, Elsevier Academic Press, ISBN: 0-12-354016-X, 2004.
- Hoskins, B. J.: The mathematical theory of frontogenesis. *Annual Reviews of Fluid Mechanics*, 14, 131–151, 1982.
- Kantha, L. H., and Clayson, C. A.: An improved mixed-layer model for geophysical applications. *Journal of Geophysical Research*, 99, 25235–25266, 1994.
- Klymak, J. M., Shearman, R. K., Gula, J., Lee, C. M., D’Asaro, E. A., Thomas, L. N., Harcourt, R. R., Shcherbina, A. Y., Sundermeyer, M. A., Molemaker, J., and McWilliams, J. C.: Submesoscale streamers exchange water on the north wall of the Gulf Stream. *Geophysical Research Letters*, 43, 1226–1233, doi: 10.1002/2015GL067152, 2016.
- 25 Large, W. G., McWilliams, J. C., and Doney, S. C.: Oceanic vertical mixing: a review and a model with a nonlocal boundary layer parameterization. *Reviews in Geophysics*, 32, 363–403, 1994.
- Lévy, M., Ferrari, R., Franks, P. J. S., Martin, A. P., Rivière, P.: Bringing physics to life at the mesoscale. *Geophysical Research Letters*, 39, L14602, doi: 10.1029/2012GL052756, 2012.
- 30 Leppäranta, M., and Myrberg, K. (Eds.): *Physical Oceanography of the Baltic Sea*. Springer, Berlin, ISBN 978-3-540-79702-9, 2009.
- Magaard, L., and Rheinheimer, G. (Eds.): *Meereskunde der Ostsee*. Springer-Verlag, Berlin, 269 pp, 1974.
- Mahadevan, A.: The impact of submesoscale physics on primary productivity of plankton. *Annual Review of Marine Science*, 8, 161–184, doi: 10.1146/annurev-marine-010814-015912, 2016.
- 35 Mahadevan, A., Tandon, A., and Ferrari, R.: Rapid changes in mixed layer stratification driven by submesoscale instabilities and winds. *Journal of Geophysical Research*, 115, C03017, doi: 10.1029/2008JC005203, 2010.
- Marmorino, G. O., Smith, G. B., and Miller, W. D.: Surface imprints of water-column turbulence: a case study of tidal flow over an estuarine sill. *Remote Sensing*, 5, 3239–3258, doi: 10.3390/rs5073239, 2013.



- Marmorino, G. O., Smith, G. B., North, R. P., and Baschek, B.: Application of airborne infrared remote sensing to the study of ocean submesoscale eddies. *Frontiers in Mechanical Engineering*, 4(10), doi: 10.3389/fmech.2018.00010, 2018.
- Marchesiello, P., McWilliams, J. C., and Shchepetkin, A. F.: Open boundary conditions for long-term integration of regional ocean models. *Ocean Modelling*, 3, 1–20, 2001.
- 5 Margules, M.: Über Temperaturschichtung in stationär bewegter und in ruhender Luft. *Meteorologische Zeitschrift*, Hann-Volume, 243–254, 1906. Translated and edited by Volken, E., Giesche, A., and Brönnimann, S.: On temperature stratification in resting and non-accelerated moving air. *Meteorologische Zeitschrift*, 25, 6, 795–804, doi: 10.1127/metz/2016/0833, 2016.
- McWilliams, J. C.: Fluid dynamics at the margin of rotational control. *Environmental Fluid Mechanics*, 8, 441–449, doi: 10.1007/s10652-008-9081-8, 2008.
- 10 McWilliams, J. C.: Submesoscale currents in the ocean. *Proceedings of the Royal Society A 472*: 20160117, doi: 10.1098/rspa.2016.0117, 2016.
- McWilliams, J. C.: Submesoscale surface fronts and filaments: secondary circulation, buoyancy flux, and frontogenesis. *Journal of Fluid Mechanics*, 823, 391–432, doi: 10.1017/jfm.2017.294, 2017.
- McWilliams, J. C., Molemaker, M. J., and Olafsdottir, E. I.: Linear fluctuation growth during frontogenesis. *Journal of Physical Oceanography*, 39, 3111–3129, doi: 10.1175/2009JPO4186.1, 2009.
- 15 Molemaker, M. J., McWilliams, J. C., and Dewar, W. K.: Submesoscale instability and generation of mesoscale anticyclones near a separation of the California Undercurrent. *Journal of Physical Oceanography*, 45, 613–629, doi: 10.1175/JPO-D-13-0225.1, 2015.
- Müller, P., McWilliams, J. C., and Molemaker, J.: The 2D/3D turbulence conundrum. In: Baumert, H. Z., Simpson, J., and Sündermann, J. (eds.) *Marine Turbulence: theories, observations and models*. Cambridge University Press, Cambridge, 397–505, 2008.
- 20 Munk, W., Armi, L., Fischer, K., and Zachariasen, F.: Spirals on the sea. *Proceedings of the Royal Society A*, 456, 1217–1280, 2000.
- Nagai, T., Tandon, A., and Rudnick, D. L.: Two-dimensional ageostrophic secondary circulation at ocean fronts due to vertical mixing and large-scale deformation. *Journal of Geophysical Research*, 111, C09038, doi: 10.1029/2005JC002964, 2006.
- Ohlmann, J. C., Molemaker, M. J., Baschek, B., Holt, B., Marmorino, G., and Smith, G.: Drifter observations of submesoscale flow kinematics in the coastal ocean. *Geophysical Research Letters*, 44, 330–337, doi: 10.1002/2016GL071537, 2017.
- 25 Onken, R.: Mesoscale upwelling and density finestructure in the seasonal thermocline – a dynamical model. *Journal of Physical Oceanography*, 22, 11, 1257–1273, 1992.
- Onken, R.: Validation of an ocean shelf model for the prediction of mixed-layer properties in the Mediterranean Sea west of Sardinia. *Ocean Science*, 13, 235–257, doi: 10.5194/os-13-235-2017, 2017.
- Osínski, R., Rak, D., Walczowski, W., and Piechura, W.: Baroclinic Rossby radius of deformation in the southern Baltic Sea. *Oceanologia*, 30 52(3), 417–429, 2010.
- Pallàs-Sanz, E., Johnston, T. M. S., and Rudnick, D. L.: Frontal dynamics in a California Current System shallow front: 1. Frontal processes and tracer structure. *Journal of Geophysical Research*, 115, C12067, doi: 10.1029/2009JC006032, 2010.
- Parks, A. B., Shay, L. K., Johns, W. E., Martinez-Pedraja, J., and Gurgel, K.-W.: HF radar observations of small-scale surface current variability in the Straits of Florida. *Journal of Geophysical Research*, 114, C08002, doi: 10.1029/2008JC005025, 2009.
- 35 Persson, A.: The Coriolis force and the geostrophic wind (Coriolis Part 5). *Weather*, 56, 267–272, doi: 10.1002/j.1477-8696.2001.tb06589.x, 2001.
- Plougonven, R., and Snyder, C.: Inertia-gravity waves spontaneously generated by jets and fronts. Part I: Different baroclinic life cycles. *Journal of the Atmospheric Sciences*, 64, 2502–2520, doi: 10.1175/JAS3953.1, 2007.



- Pollard, R. T., and Regier, L. A.: Vorticity and vertical circulation at an ocean front. *Journal of Physical Oceanography*, 22, 609–625, 1992.
- Rhines, P. B.: Geostrophic turbulence. *Annual Review of Fluid Mechanics*, 11, 401–441, 1979.
- Rudnick, D. L.: Intensive surveys of the Azores front 2. Inferring the geostrophic and vertical velocity fields. *Journal of Geophysical Research*, 101, C7, 16291–16303, 1996.
- 5 Shakespeare, C. J., and Taylor, J. R.: The spontaneous generation of inertia-gravity waves during frontogenesis forced by large strain: theory. *Journal of Fluid Mechanics*, 757, 817–853, doi: 10.1017/jfm.2014.514, 2014.
- Shchepetkin, A. F., and Williams, J. C.: A family of finite-volume methods for computing pressure gradient force in an ocean model with a topography-following vertical coordinate. Available at <http://www.atmos.ucla.edu/~alex/ROMS/pgf1A.ps>, 24 pp., last access 10 March 2017, 2001.
- 10 Shchepetkin, A. F., and McWilliams, J. C.: The Regional Ocean Modeling System (ROMS): A split-explicit, free-surface, topography following coordinates ocean model. *Ocean Modelling*, 9, 347–404, doi: 10.1016/j.ocemod.2004.08.002, 2005.
- Shcherbina, A., D’Asaro, E., Lee, C., Klymak, J., Molemaker, M., and McWilliams, J. C.: Statistics of vertical vorticity, divergence, and strain in a developed submesoscale turbulence field. *Geophysical Research Letters*, 40, 4706–4711, doi: 10.1002/grl.50919, 2013.
- Shcherbina, A., Sundermeyer, M. A., Kunze, E., D’Asaro, E., Badin, G., Birch, D., Brunner-Suzuki, A.-M. E. G., Callies, J., Kuebel Cervantes, B. T., Claret, M., Concannon, B., Early, J., Ferrari, R., Goodman, L., Harcourt, R. R., Klymak, J. M., Lee, C. M., Lelong, M.-P., Devine, M. D., Lien, R.-C., Mahadevan, A., McWilliams, J. C., Molemaker, M. J., Mukherjee, S., Nash, J. D., Özgökmen, T., Pierce, S. D., Ramachandran, S., Samelson, R. M., Sanford, T. B., Shearman, R. K., Skillingstad, E. D., Smith, K. S., Tandon, A., Taylor, J. R., Terray, E. A., Thomas, L. N., and Ledwell, J. R.: The LatMix Summer Campaign, *Bulletin of the American Meteorological Society*, 96(8), 1257–1279, doi: 10.1175/BAMS-D-14-00015.1, 2015.
- 20 Song, Y. and Haidvogel, D. B.: A semi-implicit ocean circulation model using a generalized topography-following coordinate system. *Journal of Computational Physics*, 115, 1, 228–244, 1994.
- Stamper, M. A., and Taylor, J. R.: The transition from symmetric to baroclinic instability in the Eady model. *Ocean Dynamics*, 67, 65–80, doi: 10.1007/s10236-016-1011-6, 2017.
- Sullivan, P. P., and McWilliams, J. C.: Frontogenesis and frontal arrest of a dense filament in the oceanic surface boundary layer. *Journal of Fluid Mechanics*, 837, 341–380, doi: 10.1017/jfm.2017.833, 2018.
- 25 Suzuki, N., Fox-Kemper, B., Hamlington, P. E., and Van Roekel, L. P.: Surface waves affect frontogenesis. *Journal of Geophysical Research Oceans*, 121, 3597–3624, doi: 10.1002/2015JC011563, 2016.
- Taylor, J. R., and Ferrari, R.: On the equilibrium of a symmetrically unstable front via a secondary shear instability. *Journal of Fluid Mechanics*, 22, 103–113, doi: 10.1017/S0022112008005272, 2009.
- 30 Thomas, L. N., Tandon, A., and Mahadevan, A.: Submesoscale processes and dynamics. In: Hecht, M.W., and Hasumi, H. (Eds.) *Ocean Modeling in an Eddy Regime*, *Geophysical Monograph Series*, 177, 17–38, doi: 10.1029/177GM04, 2008.
- Thomas, L. N., Taylor, J. R., Ferrari, R., and Joyce, T. M.: Symmetric instability in the Gulf Stream. *Deep-Sea Research II*, 91, 96–110, doi: 10.1016/j.dsr2.2013.02.025, 2013.
- Thompson, L.: Ekman layers and two-dimensional frontogenesis in the upper ocean. *Journal of Geophysical Research*, 105, C3, 6437–6451, 35 2000.
- Umlauf, L., and Burchard, H.: A generic length-scale equation for geophysical turbulence models. *Journal of Marine Research*, 61, 235–265, 2003.
- Wilcox, D. C.: Reassessment of the scale-determining equation for advanced turbulence models. *AIAA Journal*, 26, 1299–1310, 1988.



Zhong, Y., Bracco, A., Tian, J., Dong, J., Zhao, W., and Zhang, Z.: Observed and simulated submesoscale vertical pump of an anticyclonic eddy in the South China Sea. *Scientific Reports*, 7:44011, doi: 10.1038/srep44011, 2017.



Table 1. Parameter settings and used equations common to all ROMS setups.

* as described by Onken (2017)

Parameter	Units	Value	Meaning
K	1	10	number of vertical layers
V_{tr}	N/A	2	transformation equation
V_{str}	N/A	1	stretching function
θ_s	1	5	surface control parameter
θ_b	1	0.4	bottom control parameter
h_c	m	10	critical depth
A_V^T	m^2s^{-1}	4×10^{-5}	vertical mixing coefficient for tracers*
A_V^M	m^2s^{-1}	1×10^{-5}	vertical mixing coefficient for momentum*
Δt_{fast}	1	20	Number of barotropic time-steps between each baroclinic time step

Table 2. Parameter settings and properties of the R500 and R100 setups.

Parameter/Property	Units	R500	R100	Meaning
Δx	m	500	100	nominal zonal grid size
Δy	m	500	100	nominal meridional grid size
lon_{west}		13°30' W	14°12' W	western boundary of model domain
lon_{east}		16°30' W	15°48' W	eastern boundary of model domain
lat_{south}		53°54' N	54°18' N	southern boundary of model domain
lat_{north}		55°30' N	55°12' N	northern boundary of model domain
N_x	1	386	1033	number of tracer grid points (zonal)
N_y	1	356	1004	number of tracer grid points (meridional)
domain size	km^2	193×178	103×100	
Δt	s	150	30	baroclinic time step
A_H^T	m^4s^{-1}	5×10^5	10^3	bi-harmonic eddy diffusivity coefficient
A_H^M	m^4s^{-1}	10^3	N/A	bi-harmonic eddy viscosity coefficient
A_H^M	m^2s^{-1}	N/A	10^{-2}	mono-harmonic eddy viscosity coefficient
vertical mixing scheme	N/A	GLS	KPP	
rx_0	1	0.16	0.07	stability condition after Haidvogel et al. (2000)
rx_1	1	1.75	0.84	stability condition after Haney (1991)

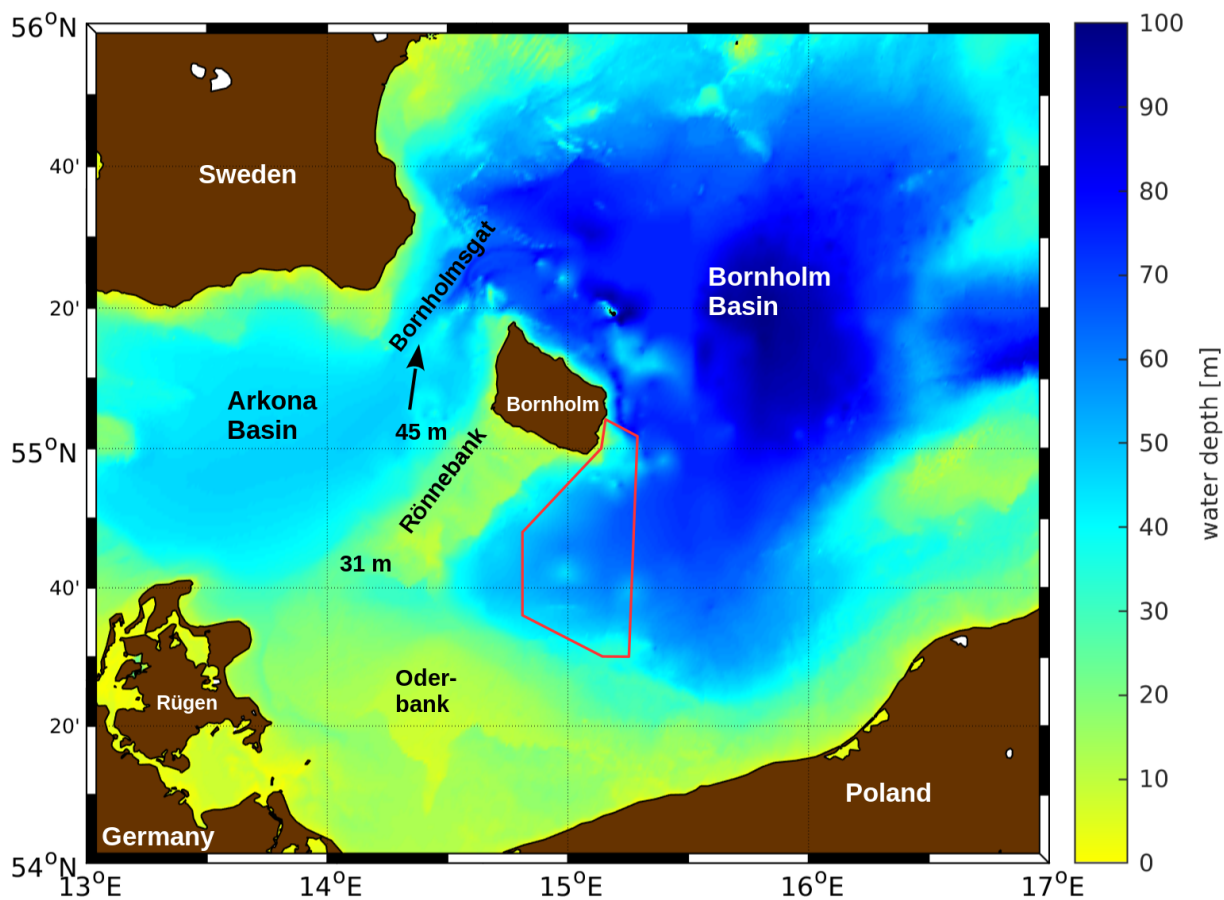


Figure 1. The western Baltic Sea. Water depth is given in metres. The approximate experimental area of the “Expedition Clockwork Ocean” is indicated by the red polygon.

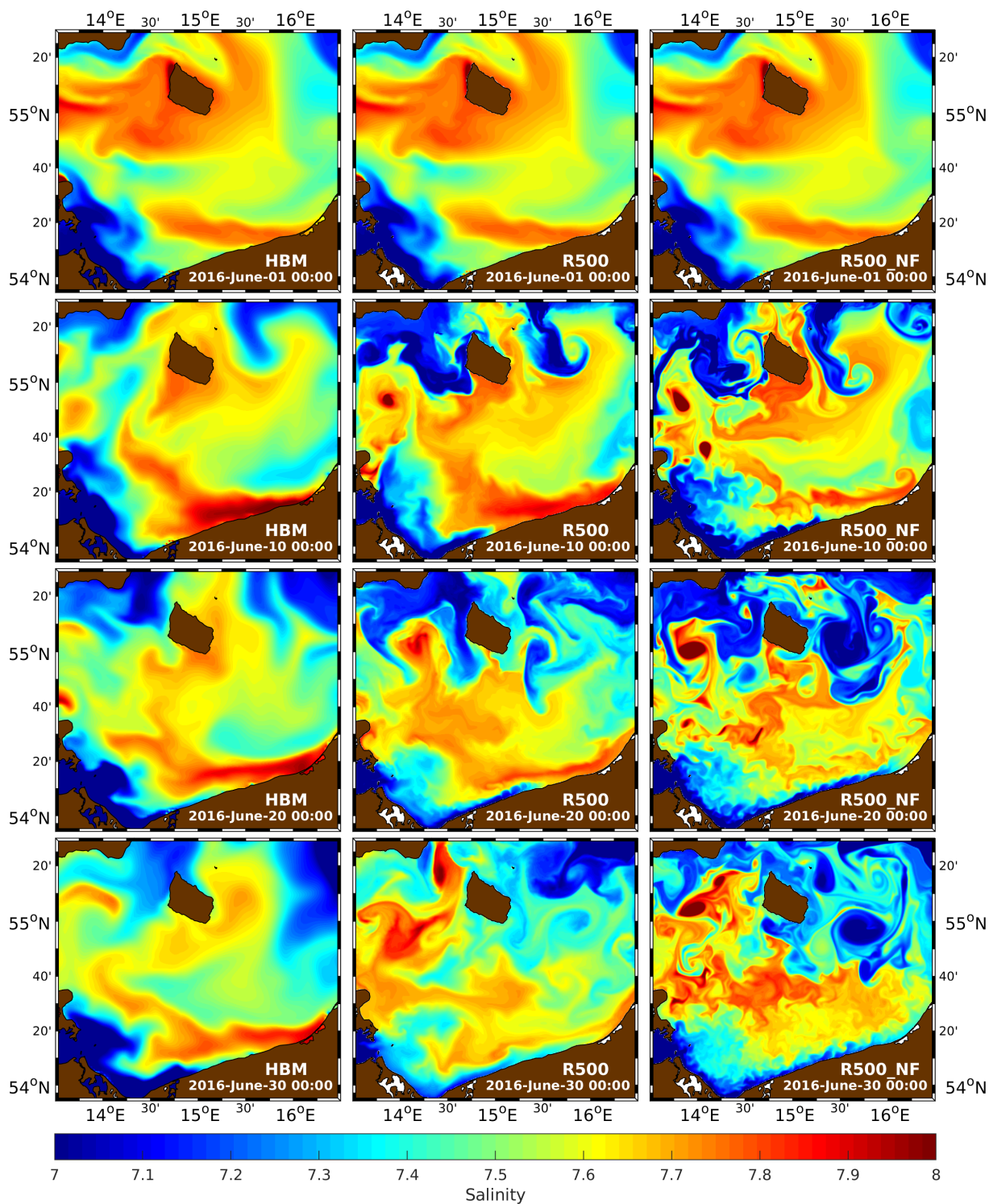


Figure 2. Top-layer salinity in HBM (left column), R500 (centre), and R500_NF (right) for 1, 10, 20, and 30 June. The HBM fields are interpolated onto the R500 horizontal grid. Due to the coarser horizontal grid of HBM, inland lakes are not resolved and salinity values were assigned to places that are dry in R500.

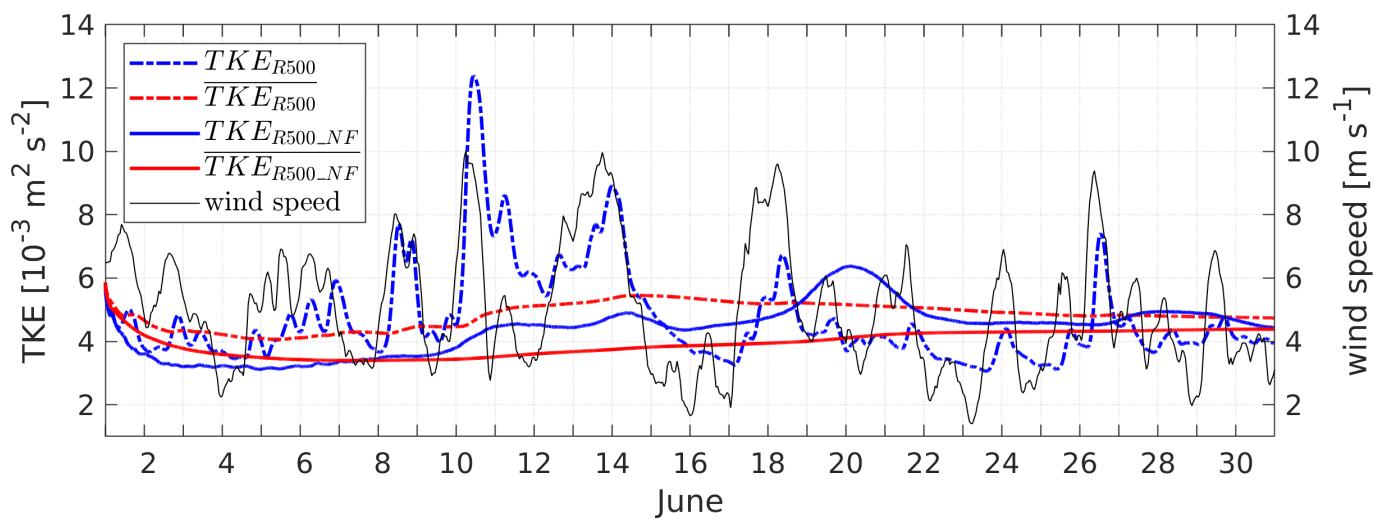


Figure 3. Instantaneous (TKE_{R500} , TKE_{R500_NF}) and cumulatively averaged ($\overline{TKE_{R500}}$, $\overline{TKE_{R500_NF}}$) total kinetic energy of the model runs R500 and R500_NF. The wind speed is shown as black curve. All quantities are averaged over the model domain.

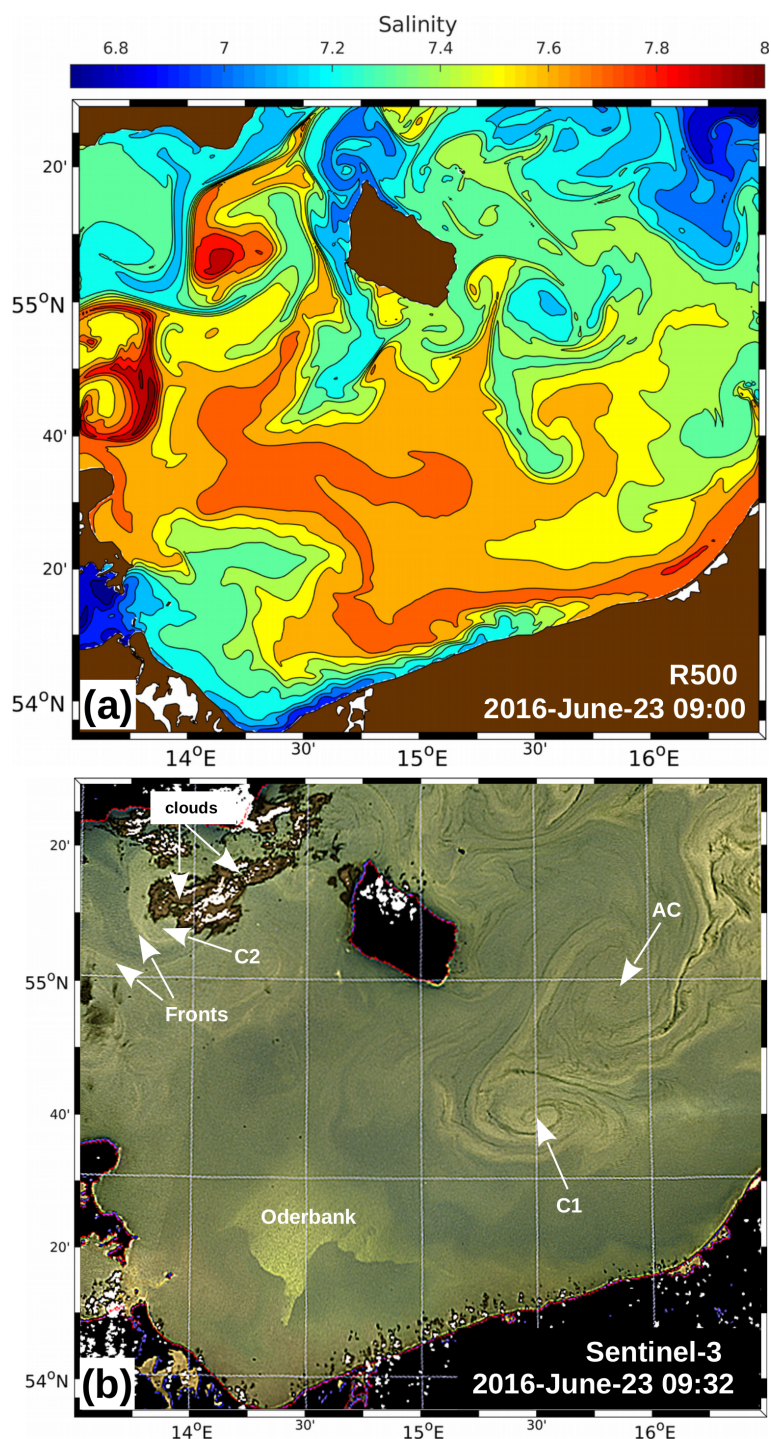


Figure 4. (a) Top-layer salinity of the R500 model on 23 June 09:00. (b) RGB composite from the Ocean and Land Colour Instrument of ESA satellite Sentinel-3 for the R500 domain on 23 June 09:32. The original image was manually adjusted in order to fit to the Mercator projection used in (a). C1, C2, and AC refer to the signatures of cyclonic and anticyclonic eddies, respectively. For the Oderbank, cf. Fig. 1.

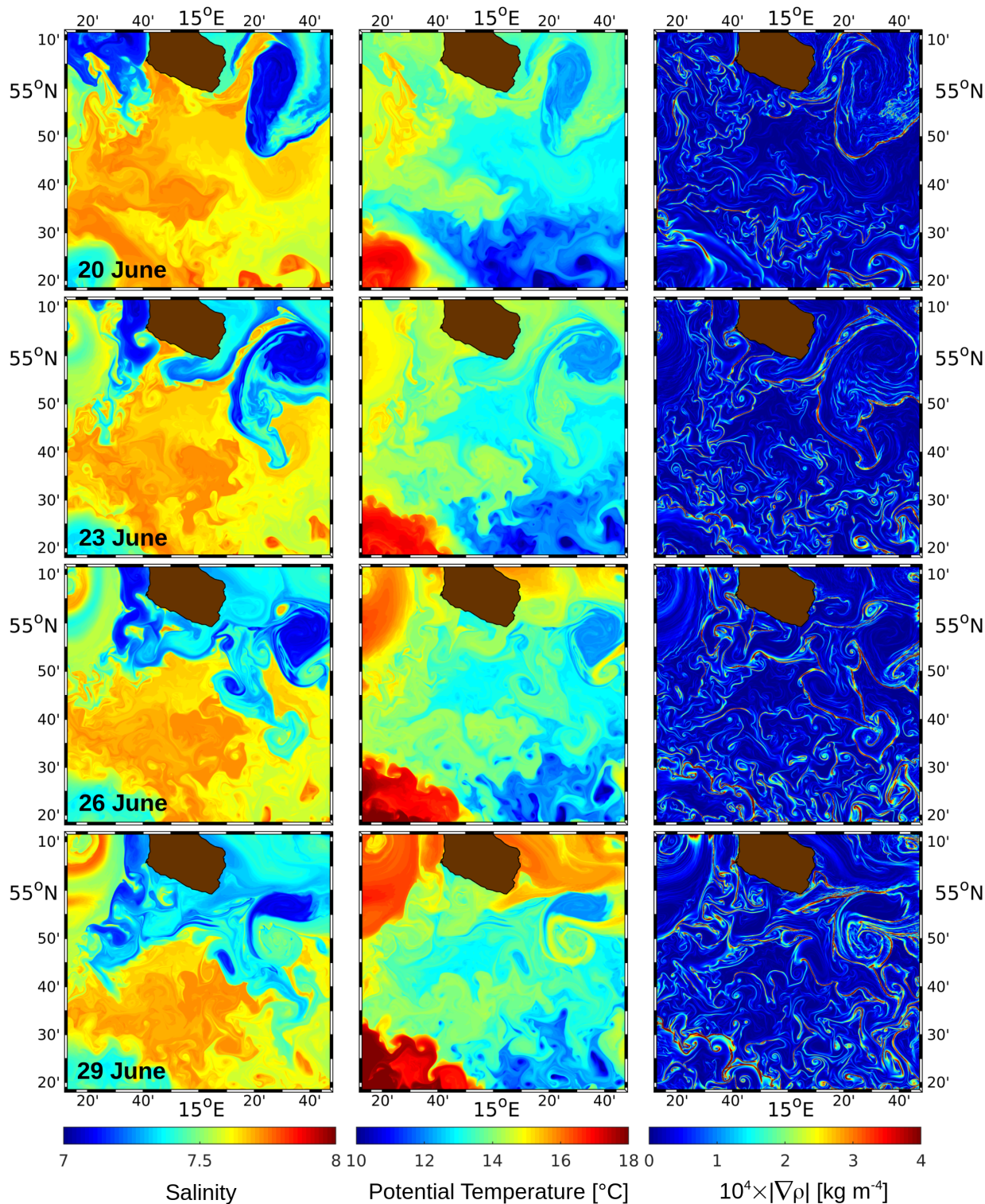


Figure 5. R100: top-layer salinity (left column), potential temperature (centre), and the absolute horizontal gradient of potential density (right) on 20, 23, 26 and 29 June. The upper end of the colour axis of $|\nabla\rho|$ is limited to 4×10^{-4} kg m⁻⁴ to distinguish higher gradients from the blue background.

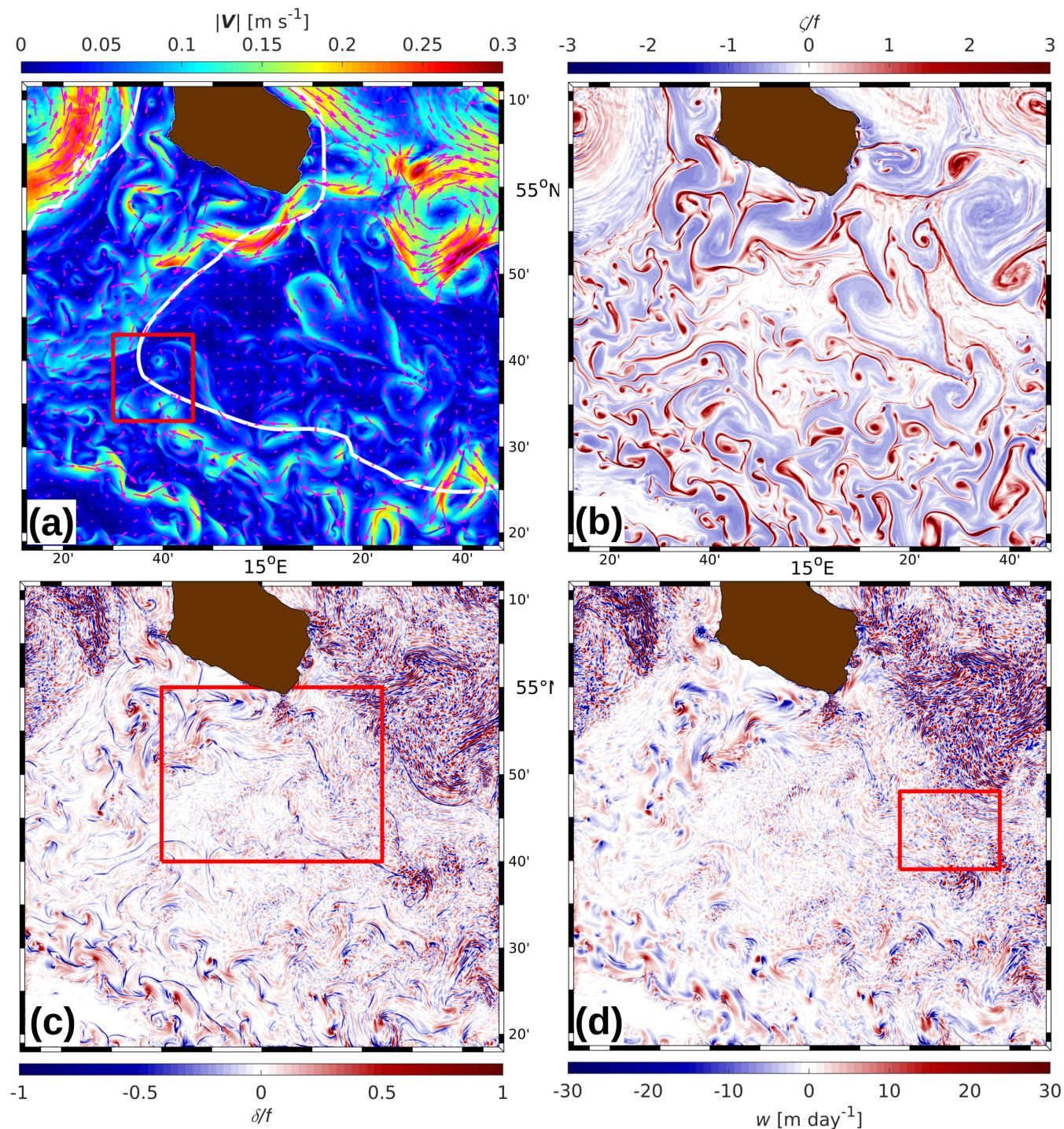


Figure 6. R100, 26 June: (a) Magnitude and direction of top-layer horizontal velocity V (vectors are plotted at 3-km resolution), (b) relative vorticity ζ and (c) horizontal divergence δ , each scaled by f , (d) vertical velocity w at 5-m depth. The white line in (a) is the 40-m depth contour. The red box in (a) refers to the zoomed area shown in Figs. 9 and 10, the box in (c) is the zoomed area of Fig. 7, and the box in (d) is the zoom shown in Fig. 13.

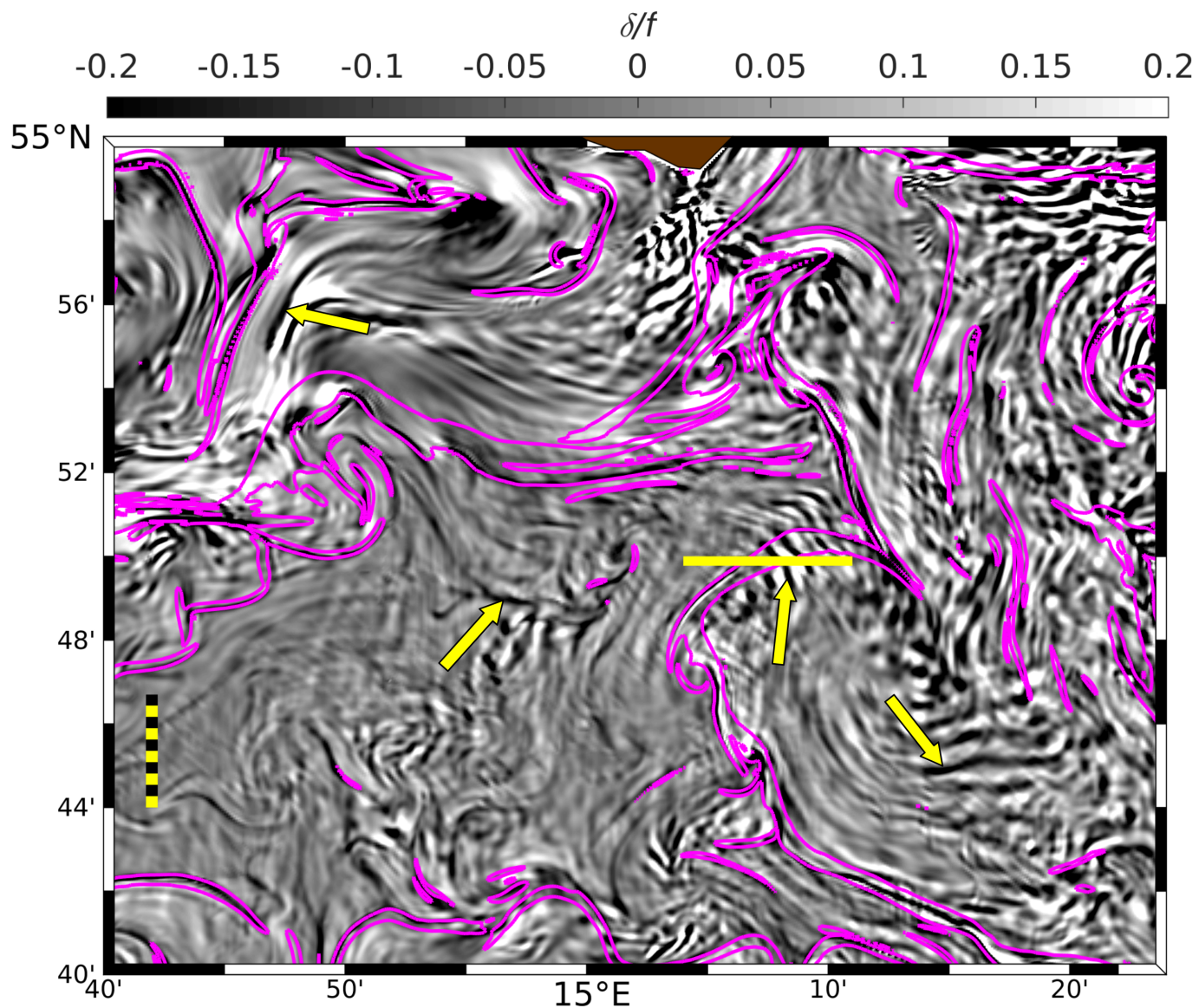


Figure 7. R100, 26 June: zoom of f -scaled horizontal divergence δ (grayscale image, for the position of the zoomed area see Fig. 6c). Bright areas indicate divergent flow, convergences appear dark. The magenta lines show the $|\nabla\rho| = 10^{-4} \text{ kg m}^{-4}$ contours. The yellow arrows likely mark internal wave packages as discussed in the text. The horizontal yellow line is the position of the section shown in Fig. 8. The black/yellow-dashed ruler represents a distance of 5 km

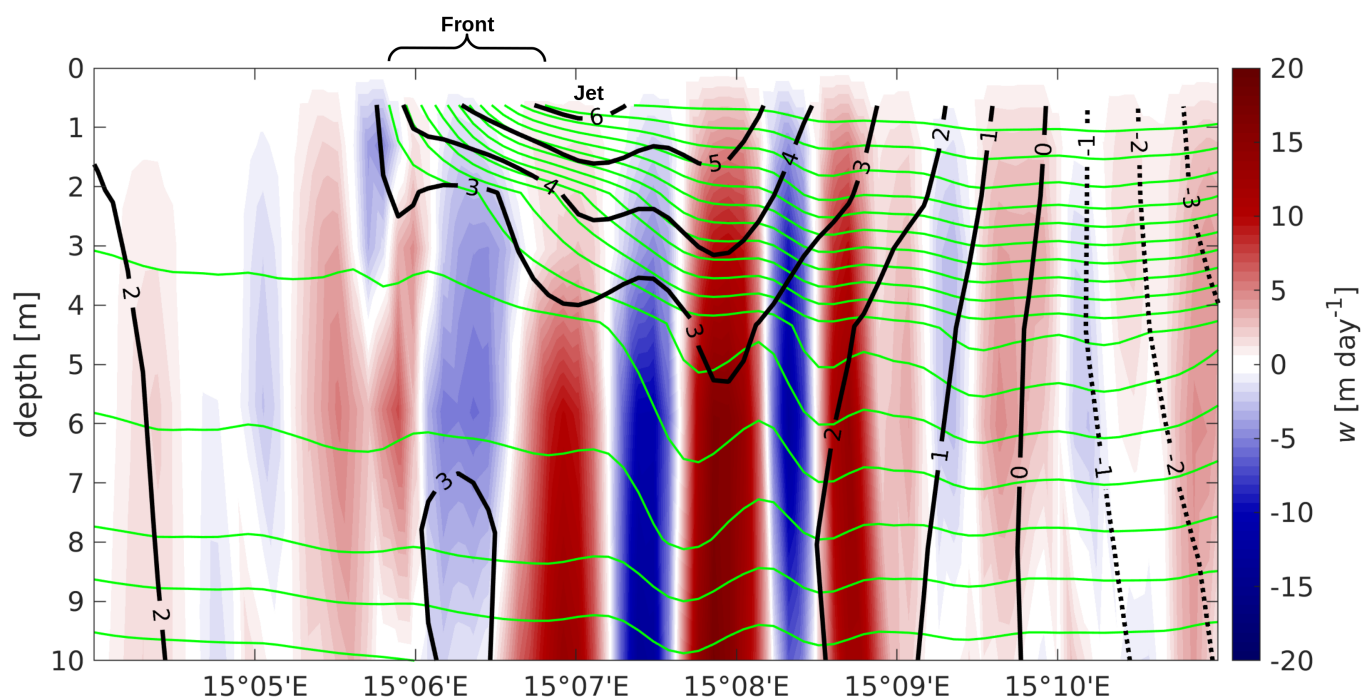


Figure 8. R100, 26 June: zonal section of vertical velocity w at $54^{\circ}49.9'$ N. Green contours indicate potential density anomaly σ_{θ} , bold solid and dotted contours are isotachs of the meridional velocity component v [cm s^{-1}]. The position of the section is marked in Fig. 7.

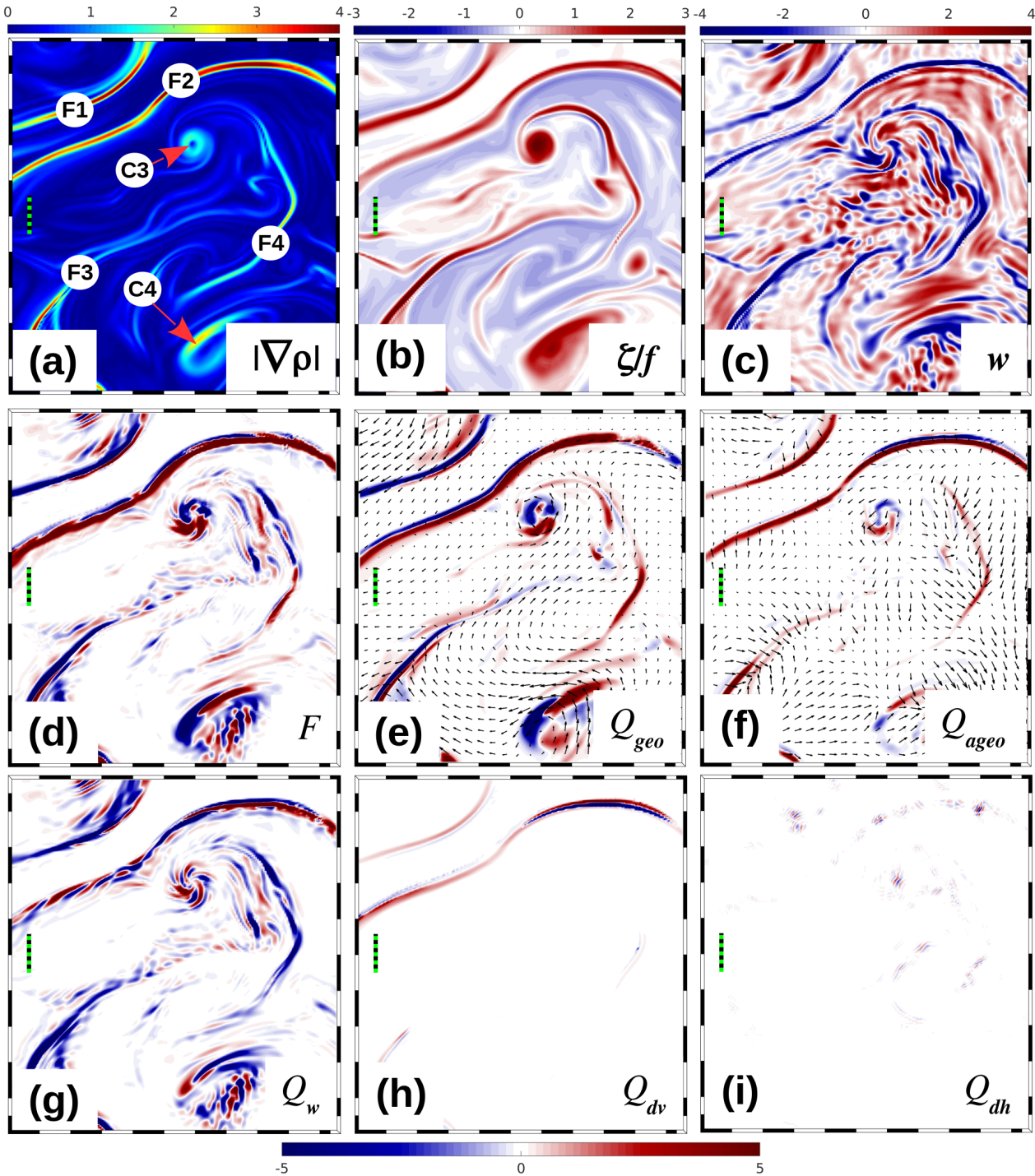


Figure 9. R100: near-surface properties on 26 June within the red box depicted in Fig. 6a. (a) Absolute horizontal density gradient $|\nabla\rho|$ [10^{-4} kg m $^{-4}$], and (b) scaled relative vorticity ζ/f in the top layer, (c) vertical velocity w [m day $^{-1}$] at the base of the top layer. (d) – (i) The frontal tendency F and the components of the tendency equation Q_{geo} , Q_{ageo} , Q_w , Q_{dv} , Q_{dh} [10^{-13} kg $^{-2}$ m $^{-8}$ s $^{-1}$] at 2-m depth. Red marks frontogenesis, blue frontolysis. For the labels F1–F4, C3, C4 see text. The black/green-dashed ruler represents a distance of 2 km, vectors in (e) and (f) are drawn at 600-m intervals.

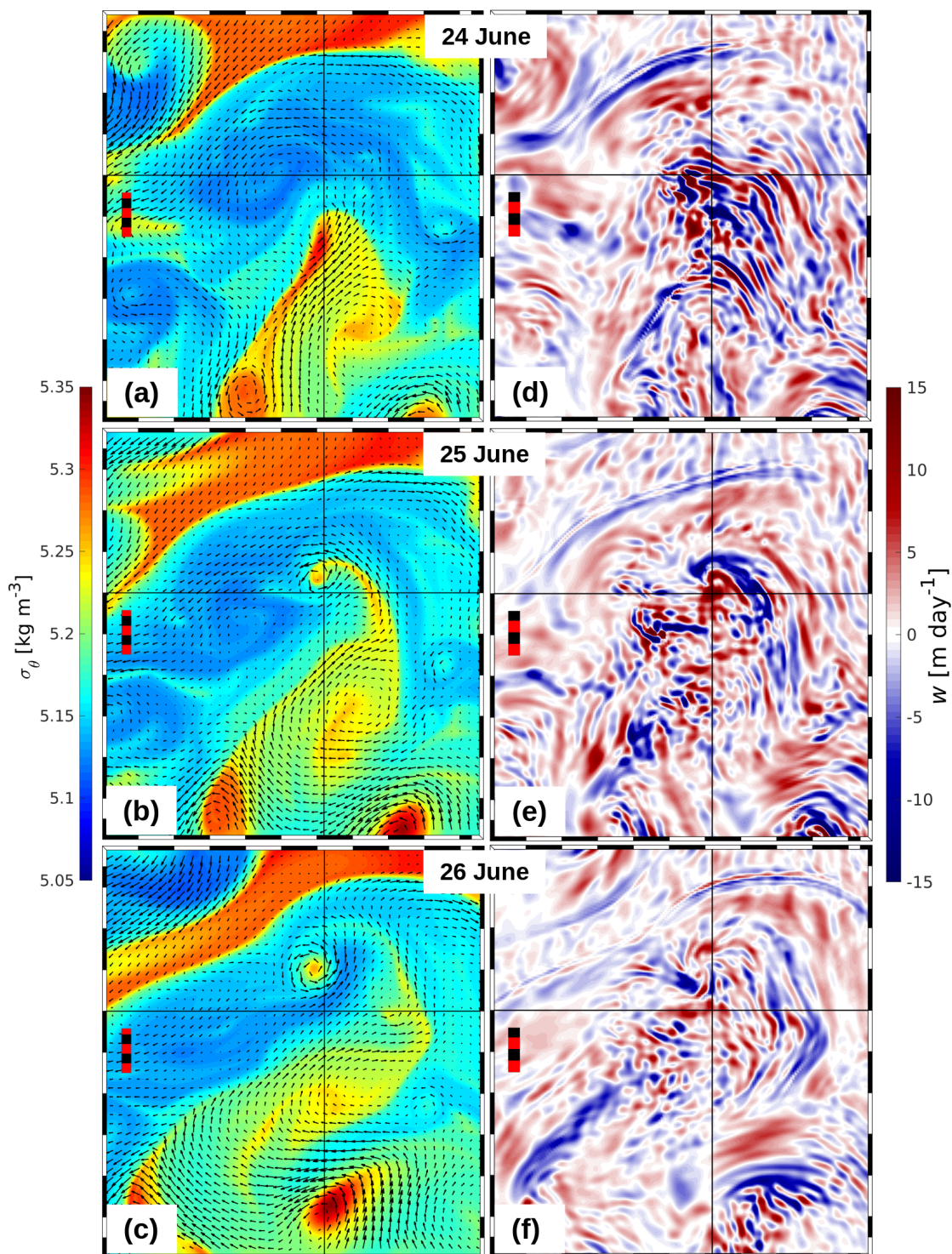


Figure 10. R100: (a)–(c) temporal evolution of potential density anomaly σ_θ in the top layer with vectors of total velocity \mathbf{V} drawn at 400-m resolution, (d)–(f) corresponding vertical velocity w at 5-m depth; upwelling is positive. The area shown is indicated by the red box in Fig. 6a. The crosshair tags the same position in all subplots. The black/red-dashed ruler represents a distance of 2 km.

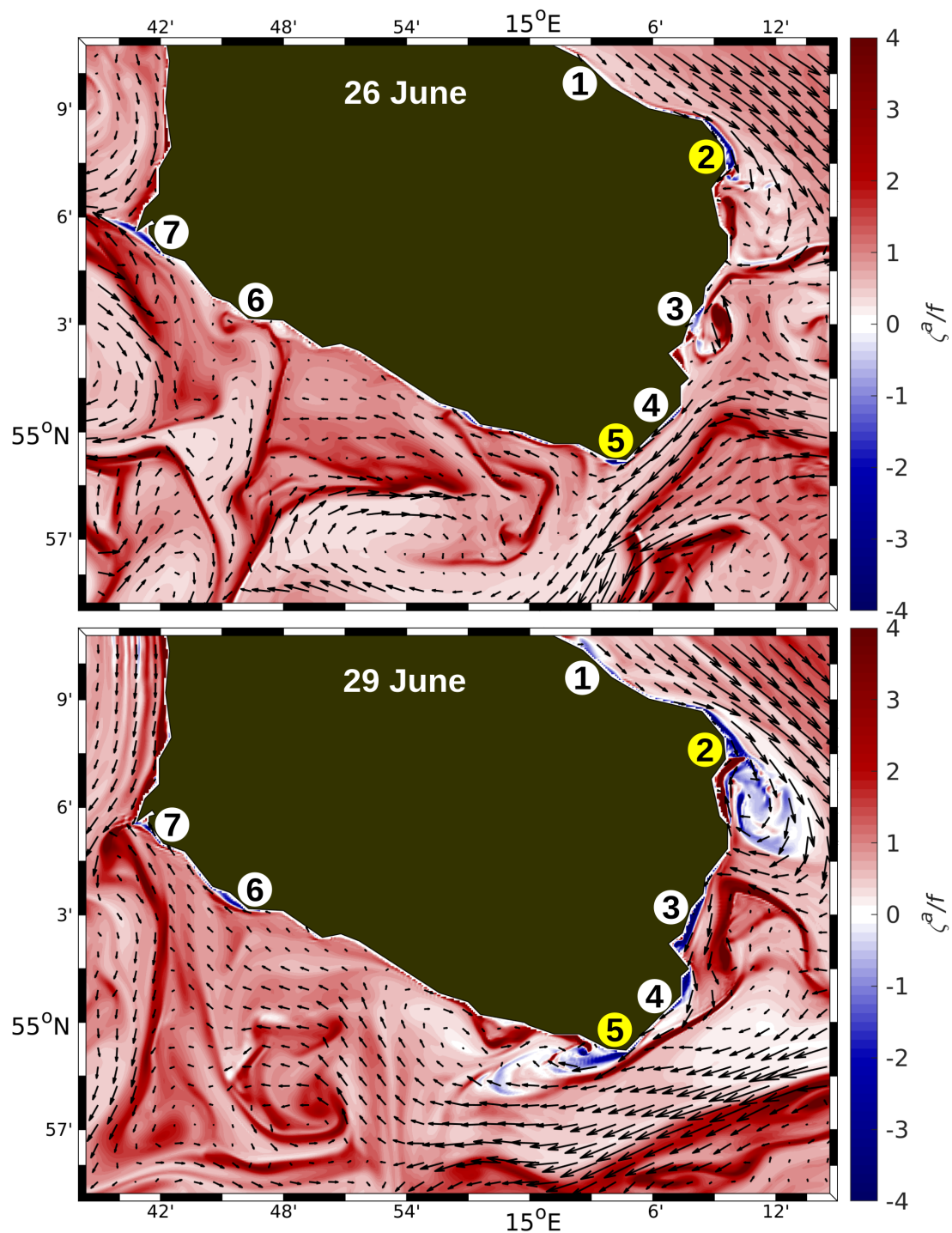


Figure 11. R100: normalized absolute vorticity, ζ^a/f , in the surface layer of the waters around Bornholm on on 26 and 29 June. Encircled numbers indicate near-coasta locations of $\zeta^a/f < 0$. Yellow circles mark locations where inertial instabilities tend to grow offshore.

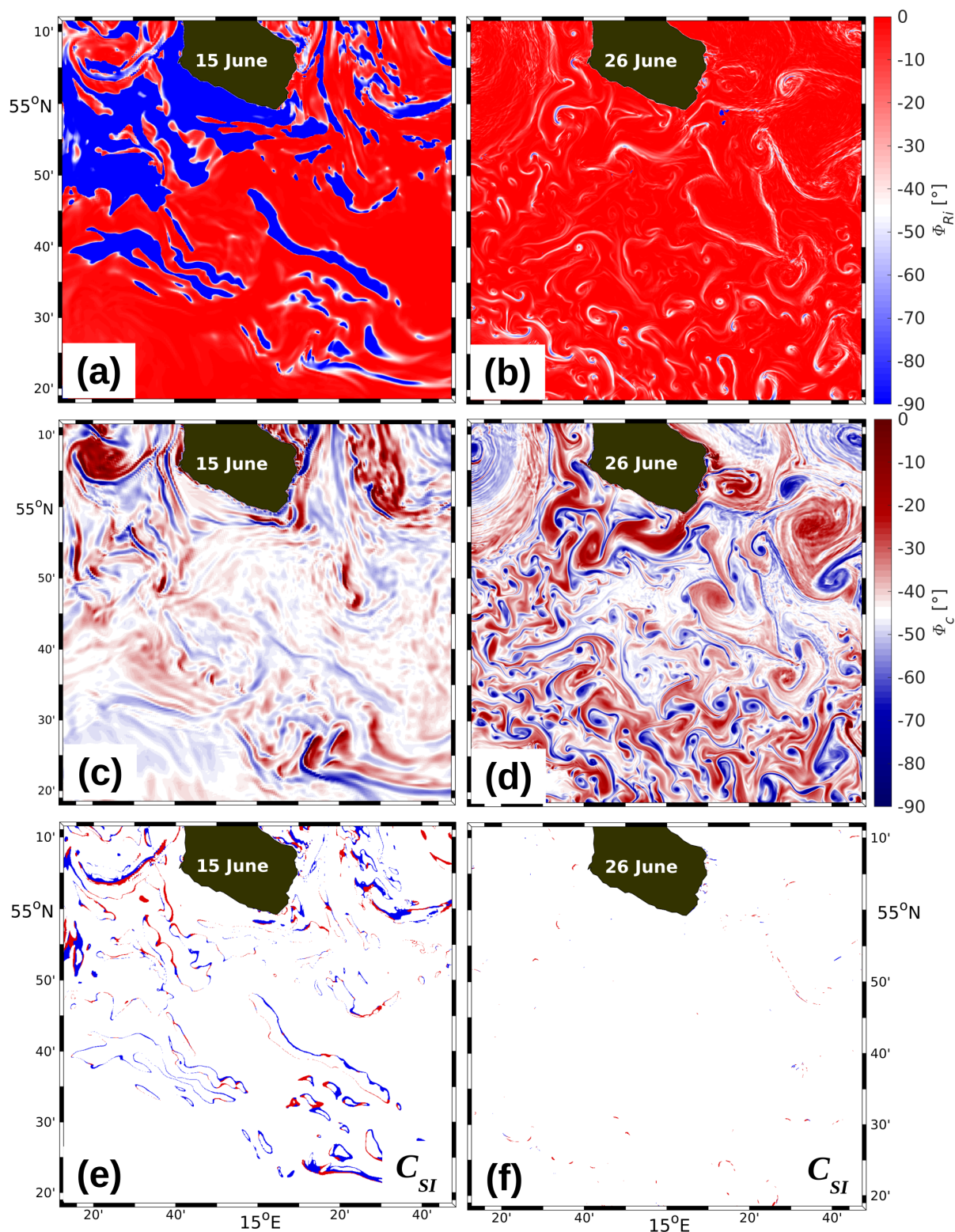


Figure 12. R100: (a, b) ϕ_{Ri} , (c, d) ϕ_c , and (e, f) C_{SI} at 3-m depth on 15 (left column) and 26 June (right). (e) and (f) are logical maps indicating where the condition for symmetric instability, C_{SI} , is satisfied in regions of cyclonic (red) and anticyclonic (blue) absolute vorticity, according to eqs. (17) and (18), respectively. For explanation of the other symbols see text.

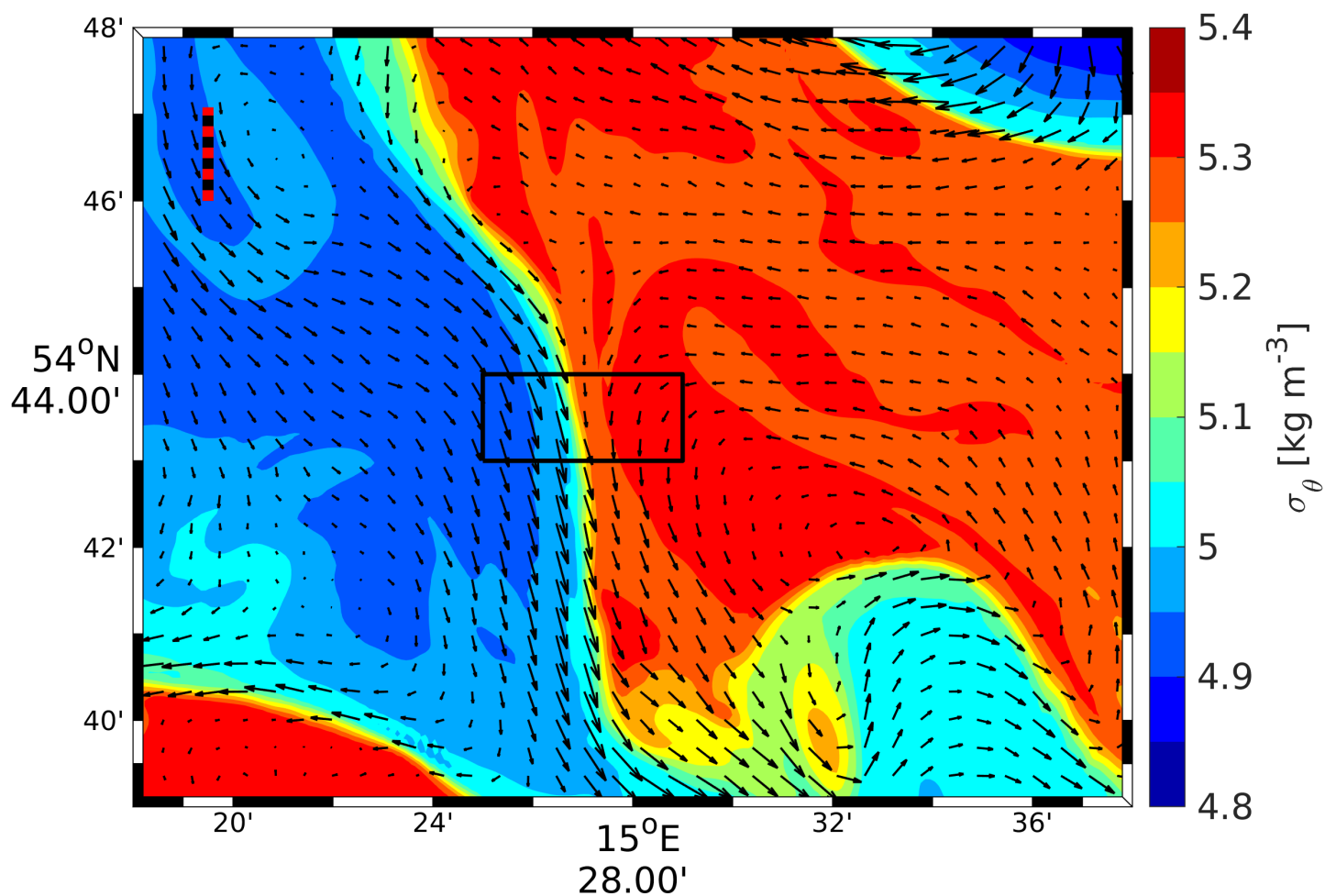


Figure 13. R100, 26 June: Potential density anomaly σ_θ in the top layer with total velocity \mathbf{V} drawn at 600-m resolution. For the position of the area, see the red box in Fig. 6d. The black box indicates the position of the maps shown in Fig. 14a–e. The black/white-dashed ruler represents a distance of 2 km.

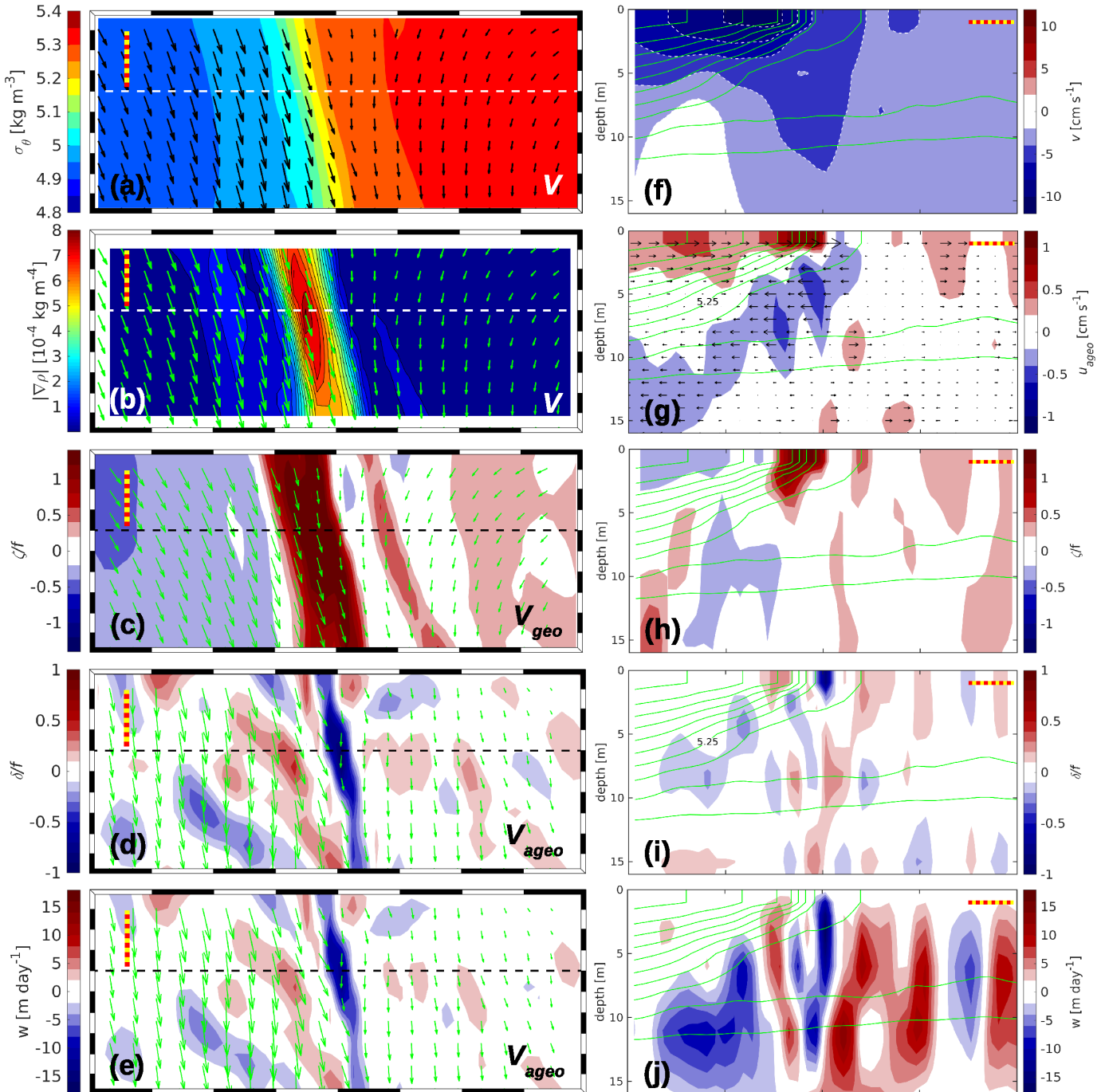


Figure 14. R100, 26 June: maps of dynamical quantities within the black box in Fig. 13. (a) σ_θ and \mathbf{V} , (b) $|\nabla\rho|$ and \mathbf{V} , (c) ζ/f and \mathbf{V}_{geo} , (d) δ/f and \mathbf{V}_{ageo} in the top layer, and (e) w and \mathbf{V}_{ageo} at the bottom of the top layer. Velocity vectors are drawn at a resolution of 200 m. Vertical sections of (f) v , (g) u_{ageo} , (h) ζ/f , (i) δ/f , and (j) w . Contour lines of potential density anomaly σ_θ are green and spaced at the same intervals as in (a). The horizontal dashed lines in the centres of (a)–(e) indicate the position of the zonal sections displayed in (f)–(j). In either subplot, the red/yellow-dashed rulers represent a horizontal distance of 500 m.

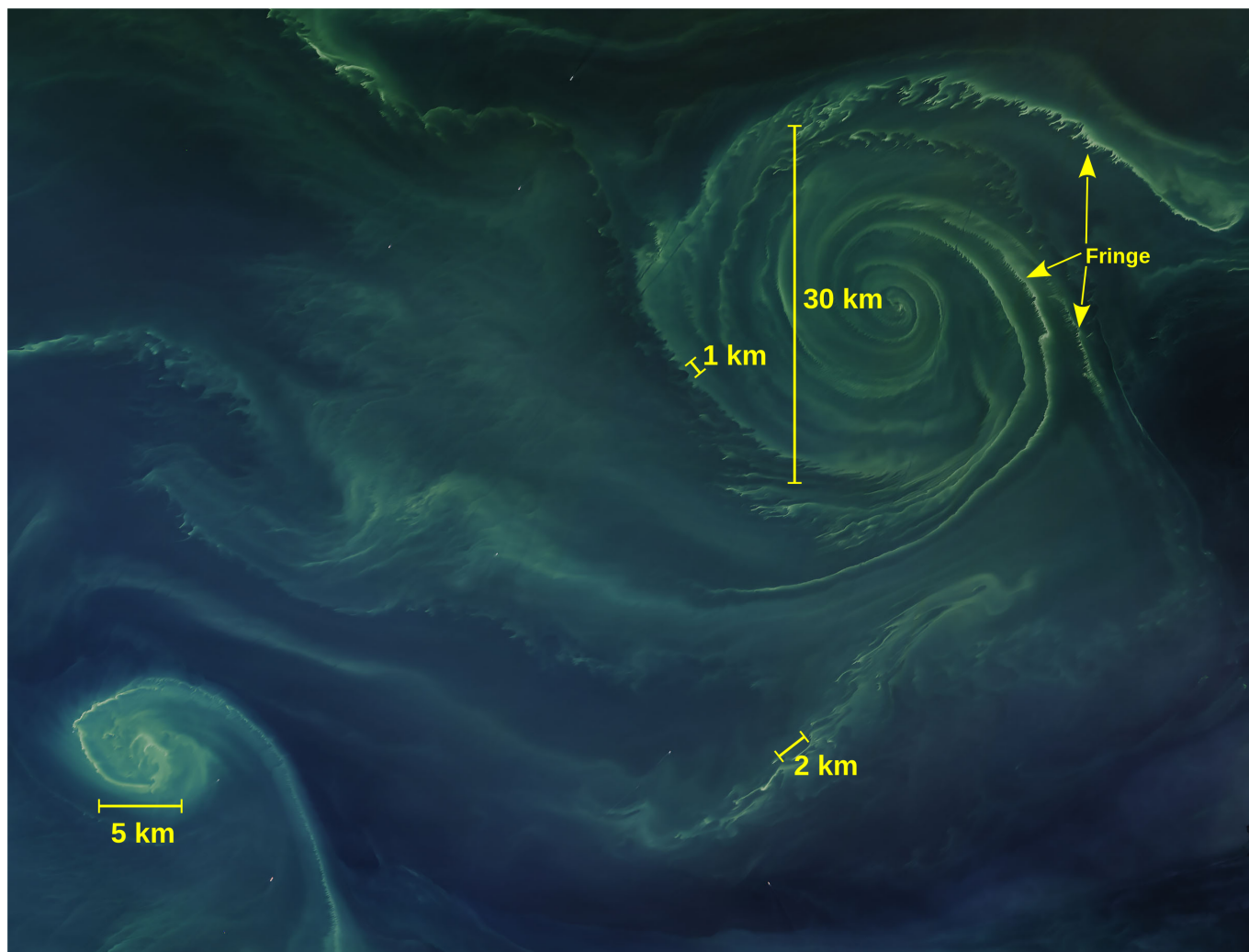


Figure 15. Phytoplankton bloom in the Baltic Sea off the Estonian coast. The natural-colour image was captured by the Operational Land Imager on NASA's Landsat 8 satellite on 18 July 2018.

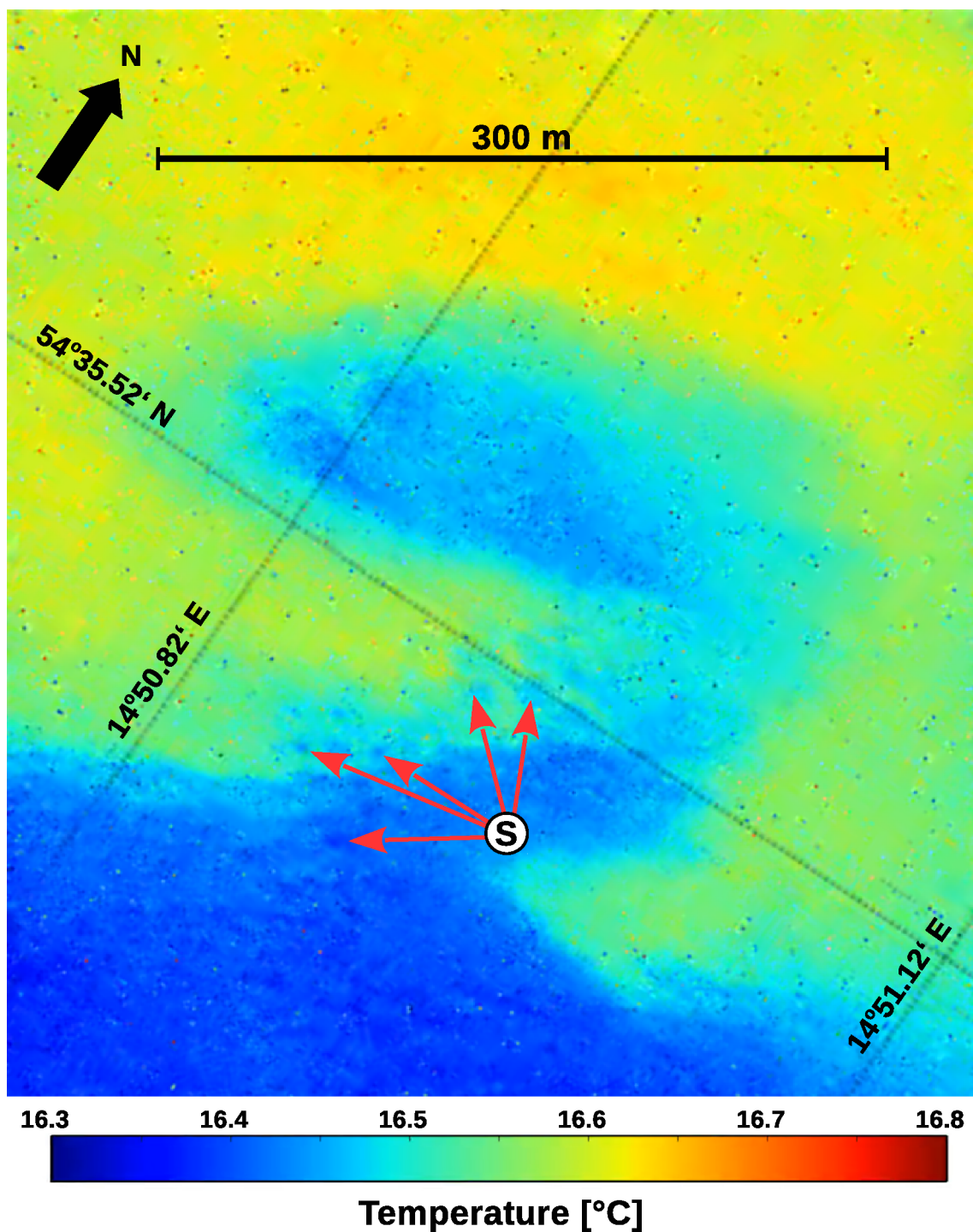


Figure 16. Sea surface temperature of a very small cyclonic eddy observed on 27 June 2016 during the “Expedition Clockwork Ocean” south of Bornholm. The image was taken with a hyperspectral camera onboard a zeppelin which “parked” over the eddy and recorded its life cycle. Cold water spots are denoted by “S”.

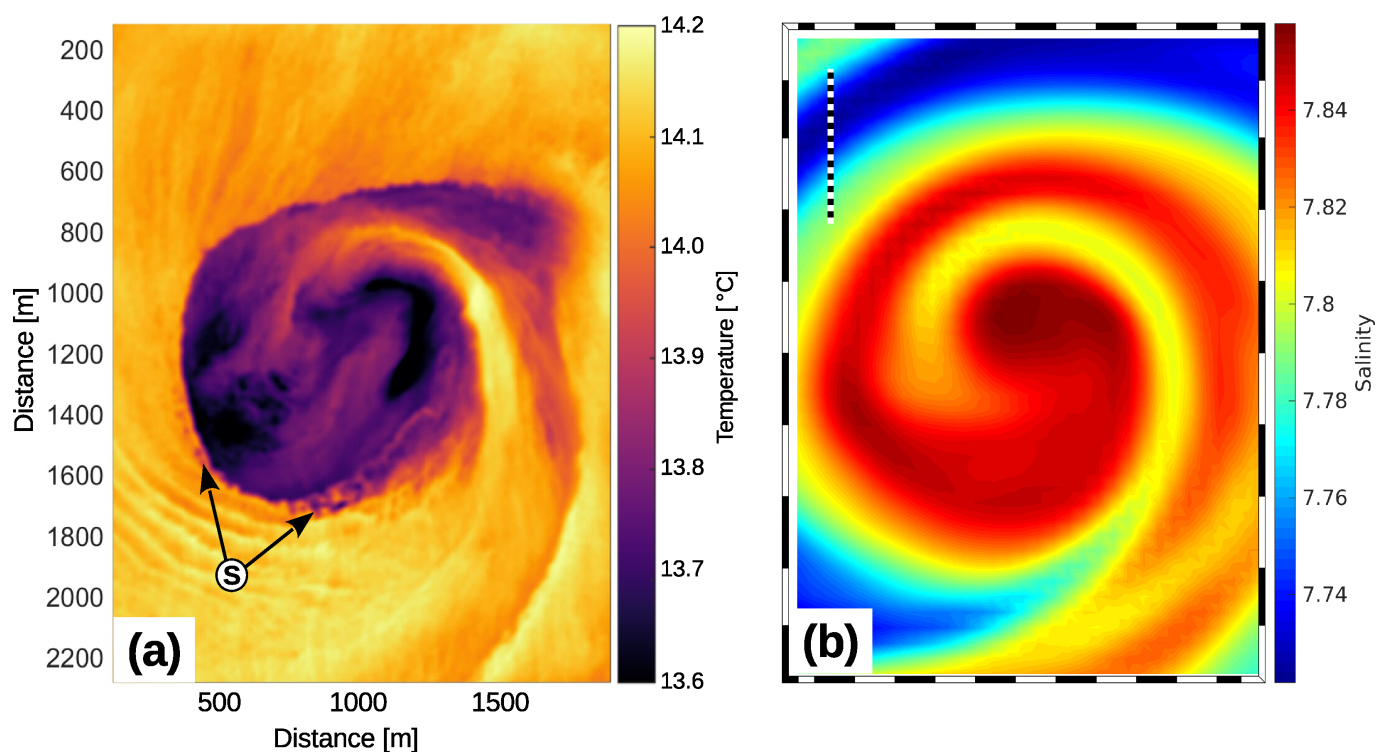


Figure 17. Passive tracer patterns of submesoscale eddies. (a) Observed sea surface temperature of a cyclonic eddy in the Southern California Counter Current. The image was taken on 1 February 2013 at 20:34 in the framework of the SubEx experiment (Marmorino et al., 2018). (b) Modelled salinity of the cyclone C3 at 15-m depth (cf. Figs. 9 and 10). Cold water spots in (a) are denoted by “S”. The black/white-dashed ruler in (b) represents a distance of 1 km.